MAGNETIC METHODS OF NONDESTRUCTIVE EVALUATION

In nondestructive evaluation (NDE), measurements are made in such a way that after the measurements are completed, the specimen is not physically altered as a result of the measurement. In the case of magnetic measurements this means that the specimen, if magnetized, can always be demagnetized and restored to its original state. A nondestructive measurement is therefore just what the label says—nondestructive.

Magnetic methods of nondestructive evaluation are used to find three major types of information: (1) detection and characterization of macroscopic flaws in a specimen such as cracks, corrosion pits, or inclusions; (2) characterization of microstructural features such as creep damage, plastic deformation, grain size, and compositional features; (3) characterization of residual stress and residual stress distribution in a specimen. In most cases, a magnetic technique is used typically for only one of these uses; in some cases, it may be used for several.

Our discussion in this review will categorize magnetic methods primarily according to the purpose for which the methods are used. Thus, the article will be divided into three major sections according to the type of information sought. Not included in our discussion will be NDE measurement techniques involving eddy currents, as such techniques are used mostly for nonmagnetic materials. A discussion of promising future magnetic NDE techniques will be included in a final major section.

Review articles on various aspects of magnetic NDE that might also be consulted are found in Refs. 1–20.

MAGNETIC METHODS FOR CRACKS, CORROSION PITS, OR INCLUSIONS

Magnetic Particle Inspection (MPI)

Magnetic particle inspection (MPI) was developed in the 1930s by Magnaflux Corporation (21). The method was based on the chance discovery that iron filings tended to collect close to flaws in steels during the grinding process. Magnaflux Corporation turned this observation into a successful commercial method of locating flaws in steels (1,21).

Magnetic particle inspection (MPI) depends on the leakage of magnetic flux at the surface of a ferromagnetic material at locations of surface-breaking or near-surface flaws (see Fig. 1). In order for the method to be effective, the magnetic material has to be magnetized in the vicinity of the flaw. This is accomplished usually in one of two ways: (1) via a magnetic field injected into a specimen by a magnetic “yoke” wound with current-carrying coils (see Fig. 2); (2) by using contact electrodes called “prods,” which inject currents directly into the specimen, in turn magnetizing the specimen. In the case of the “yoke,” the magnetic field circulates into the specimen parallel to the surface, running from one yoke pole piece to the other. Flaws in the material break up this parallel field pattern in the vicinity of the flaw to produce a field gradient and magnetic force, which holds iron filings near the flaw. With “prods,” the injected current generates a circulating magnetic field, as given by the “right-hand rule” (22). Flaws distort the field pattern, again producing field gradients and forces that hold filings near the flaws. In both cases, the best indication is given when the field is perpendicular to the largest flaw dimension, either the crack length or the most prolately shaped side of the flaw in the case of corrosion pits or inclusions.

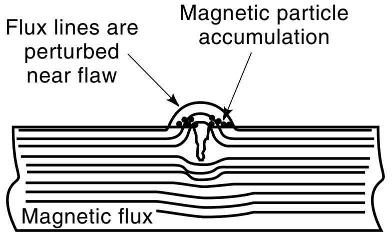

Figure 1. Magnetic particle accumulation in the leakage flux produced by a flaw (after Ref. 10).

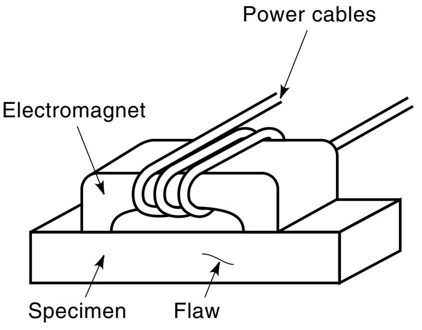

Figure 2. The yoke method for magnetizing a specimen (after Ref. 10).

The MPI method is reliable, when used correctly, for finding surface and near-surface flaws of sufficient macroscopic size and gives an indication of the location and length of the flaw. The field must be strong enough to hold the particles applied. Very shallow cracks can be missed, as can subsurface cracks, if the leakage fields are weak. The magnetic particles best used are ones that are fine enough and have a high enough permeability to be held (21). The component being tested can be almost any size or shape, although care is needed with complex geometries.

The method has limitations. For best results, the magnetic field must lie perpendicular to the flaw direction. Flaws can be overlooked by misorientation of the field or by using a field that is not strong enough to hold the particles. Finally, while the length of the flaw is obtainable, depth of flaw can only be guessed (unsatisfactorily) by the amount of powder accumulated.

Various enhancements have been added (1,10). These include wet techniques, such as water-borne suspensions known as “magnetic inks.” Also, fluorescent magnetic powders often give clearer indication of smaller flaws when viewed under ultraviolet light (23). Another method is a magnetic tape, which is placed over the area to be inspected (24). The tape is magnetized by the strong surface field, the gradients of which leave imprints of flux changes at defect locations. A quantitative flux leakage reading is obtained by inspecting the tape with a Hall probe or fluxgate magnetometer.

The tape is particularly useful in places hard to inspect by MPI.

Magnetic Flux Leakage (MFL)

As with the MPI method, the magnetic flux leakage (MFL) method depends on the perturbation of magnetic flux caused by surface or near-surface flaws. The MFL method differs from MPI in that it utilizes a flux-detecting device to detect the perturbations associated with the flaw. Another name for the MFL method is the "magnetic perturbation" (MagPert) method (7).

The MFL method offers extra information because the flux density components in three directions, parallel and perpendicular to the flaw direction and normal to the surface, can be measured. Usually, however, only components parallel to the surface are actually measured.

The method gained acceptance after a practical flux-leakage measuring system was developed (25), which was capable of detecting surface and subsurface flaws on the inner surface of steel tubes, a location unsuitable for the MPI method. The MFL technique is now even more developed in that it can be used for both detection and characterization of flaws (7, 26–28).

The leakage flux probe is usually an induction coil or a Hall probe. The probe is accompanied by a magnet that magnetizes the specimen in its vicinity. As the probe is scanned across the specimen surface, detected flux density anomalies indicate flaw location. Figure 3 shows the use of such a probe both (a) to detect a crack and (b) to detect a region of low

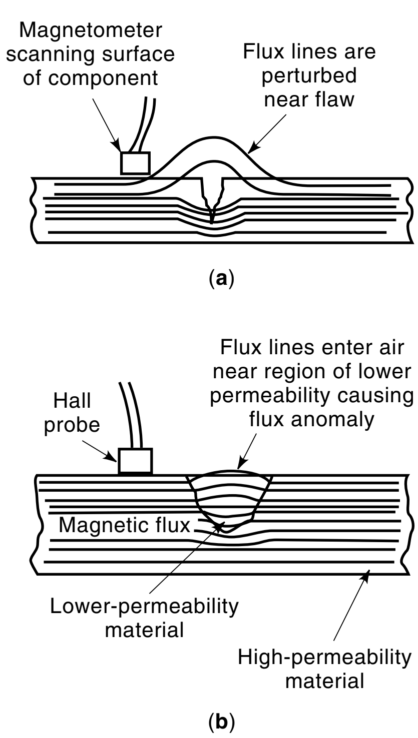

Figure 3. Using magnetic flux leakage (a) to detect flaws and (b) to detect regions of different permeability (after Ref. 10).

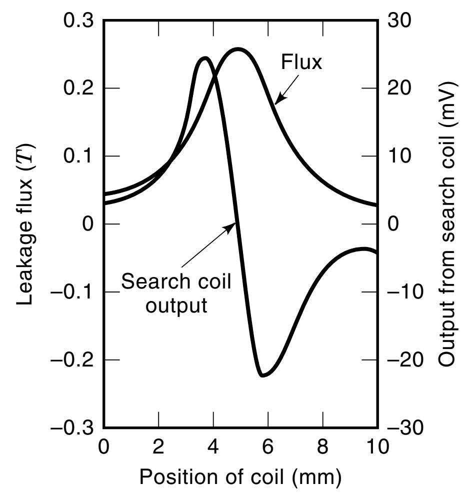

Figure 4. Leakage flux variation and search coil output with distance across a crack (after Ref. 27).

permeability. Figure 4 shows variation of leakage flux density as the probe moves across a crack and the voltage in a search coil moving at constant speed through this changing flux density (27).

The use of the search coil sensor is based on Faraday's law of induction, which states that the voltage induced in the coil is proportional to the number of turns in the coil multiplied by the time rate of change of the flux threading through the coil (7). To produce a voltage, either the coil must be in motion or the flux density must be changing as a function of time. For MFL, the moving coil is used to sense spatial changes in leakage flux. If the coil is oriented to sense flux changes parallel to the specimen surface in the direction x, then as the coil moves through the spatially perturbed flux above a flaw, the induced emf is given by (7)

$$V = N\frac{d\Phi}{dt} = NA\frac{dB_p}{dx}\frac{dx}{dt} \qquad (1)$$

where A is coil cross-sectional area, N is number of turns, B_p is flux density component parallel to the surface, dx/dt is constant coil velocity, and $d\Phi/dt$ is rate of change of magnetic flux $\Phi = B_pA$ that is threading the coil. From Eq. (1), the coil voltage V is proportional to the flux density gradient along the direction of coil motion times the coil velocity.

The Hall sensor does not detect the flux gradient, but measures directly the component of flux itself in a direction perpendicular to the sensitive area of the device (7,27). Because the Hall sensor response is not dependent on probe motion, a variable scanning speed can be used. In air, the Hall sensor is often used to measure magnetic field $H_p = B_p/\mu_0$, where μ_0 is the permeability of free space, and where the Hall sensor is oriented to measure field and flux density components parallel to the specimen surface. The Hall sensor is used to measure H_p because it has a small sensitive area that can be placed very close to the specimen surface. As H_p is continuous across the surface boundary, the H_p measured is equivalent to H_p in the specimen. The Hall sensor is more difficult to fabricate and more delicate than induction coil sensors.

The disadvantage of the MFL method, compared with MPI, is that scanning a leakage flux detection probe across the surface of a specimen can be quite time-consuming. The MPI method, on the other hand, can check large areas of a specimen quite quickly.

The MFL method is quite useful if the location of the flaw is known with a fairly high probability because the MFL method can be used to characterize flaws as to size and depth (26–28). Also, if a matrix of scanners can cover the entire surface of the specimen in one pass, the MFL method offers advantages in that it can be done systematically. This is the case when a circular ring of leakage flux scanners is placed on a "pig" inside a pipeline and is sent through the pipeline to detect corrosion and other flaws on the inside of the pipeline (29,30). For pipeline, MFL is preferred because the inside of a pipe is hard to inspect visually.

Interpretation of MFL in terms of flaw size and shape was made possible by quantitative leakage field modeling. In early papers, Shcherbinin and Zatsepin (31,32) approximated surface defects by linear magnetic dipoles and by calculating the dipole magnetic fields. In this way, expressions were obtained for both the normal and tangential components of the leakage flux density. Numerical computations fit experimental data surprisingly well. In the case of leakage fields due to inclusions and voids, a model by Sablik and Beissner (28) was developed, which approximated voids and inclusions as either prolate or oblate spheroids. Expressions for the three components of flux density were used to study the effects of oblateness and size and depth of defect. Another analysis was that of Edwards and Palmer (33), who approximated a crack as a semielliptic slot and computed the leakage flux density components and the forces on magnetic particles, so that quantitative analysis of MPI might also be tenable.

Significant progress in leakage field computation was made by Hwang, Lord, and others (34–37), who used finite element modeling methods. The leakage field profiles obtained for a simple rectangular slot agreed excellently with observation (34). Other finite element calculations (35) showed how different defect shapes and geometries affected the leakage field signals. A similar technique, finite difference modeling, was also used for computing leakage fields (38).

Reviews of leakage field calculations and interpretation of measurements have been given by Dohman (39) and Holler and Dobmann (40). These authors have discussesd both detection and sizing. Owston (41) reported on differences in leakage flux signals between fatigue cracks and artificial flaws such as saw slots, and also on leakage flux as a function of liftoff (i.e., distance of detector from specimen surface). Forster (42) has discussed the correlations of observed magnetic leakage field measurements with expectations based on finite element modeling and shown notable discrepancies.

One complication in the leakage field computations is residual stress around the defect. The residual stress produces a distribution of permeability changes about the defect, in effect creating a new magnetic geometry. This is why the leakage field of a fatigue crack differs from that of a slot. Recent papers have attempted both theoretically (43) and experimentally (44,45) to deal with the effect of residual stress on leakage field signals from corrosion pits.

A leakage field detection technique, called the electric current perturbation (ECP) technique (46,47), has also been used for nonmagnetic materials. It involves either injecting (via electrodes) or inducing (via a coil) an electric current in the vicinity of a flaw. The current passes around the defect, creating a characteristic leakage field signal in the flux density produced by the flow of current. Clearly the technique has its origins in MFL.

The MFL is used primarily by the oil and gas industry for inspections inside tubulars, such as gas pipelines, downhole casing and other steel piping (7,29,30). The cylindrical geometry aids in characterizing defects. The MFL has also been used for irregularly shaped parts, such as helicopter rotor blade D-spars (48), and for bearings and bearing races (49).

Magnetostrictive Sensors (MsS)

A relatively new technique for nondestructively locating flaws well away from the position of the sensor is called "magnetostrictive sensing" (MsS) (50,51). Current in an ac coil, axisymmetrically surrounding a steel pipe in the presence of a static axial magnetic field, generates an electromagnetic field in the pipe wall, which magnetostrictively generates oscillating strains and hence elastic waves. These elastic waves travel down the pipe wall in both directions from the coil location and reflect off defects such as corrosion pits or deep cracks. The returning reflected elastic waves magnetostrictively produce changing magnetization underneath a detector coil, also in a static axial magnetic field, and the changing magnetization induces an emf in the detector coil. The time lag between generation and detection gives information about where the defect is located, and the shape of the signal gives clues about the nature of the defect (52,53).

The technique not only offers the possibility of inspecting long sections of pipe or tubing, as much as 500 m away, but also works when there are bends and elbows in the pipe (53). The wave generation coils, sensing coils, and field coils all are suspended axisymmetrically on plastic forms around the pipe, so that the coupling of coils to the pipe does not involve direct contact (51). In addition, the inspection is volumetric and senses defects and flaws well inside the pipe wall and not just near the surface (53). Bridge cable strands (54) and concrete reinforcement bars (55) also can be inspected with the technique.

Figure 5 shows the transmitter and receiver coils on a steel pipe specimen and a block diagram showing the basic electronic circuitry. The bias magnets, operating together with transmitter and receiver coils, can be large current dc coils surrounding the ac coils. (In Fig. 5 there is one bias coil enveloping both receiver and transmitter.) The bias magnets can also be arrays of magnetic circuit modules spaced equally around the pipe (56). Figure 6 shows this latter configuration. Figure 7 shows reflected waves from welds in a pipe and from the far end of the pipe. Because second reflections of weld reflections are seen, careful interpretation is required.

Russian investigators began to consider the possibility of using magnetostrictive wave generation for sensing reflected waves from rod and pipe defects and developed theoretical models for the magnetostrictive wave generation in the long wavelength approximation (57,58). More recently, Sablik and Rubin (59) have produced a model, from which numerical results can be extracted for any frequency, without restriction. The more recent model reproduces the dispersion spectrum measured in pipes (59,60). The issue of wave amplitude and signal-in to signal-out still needs more work for a complete match with the experiment (61).

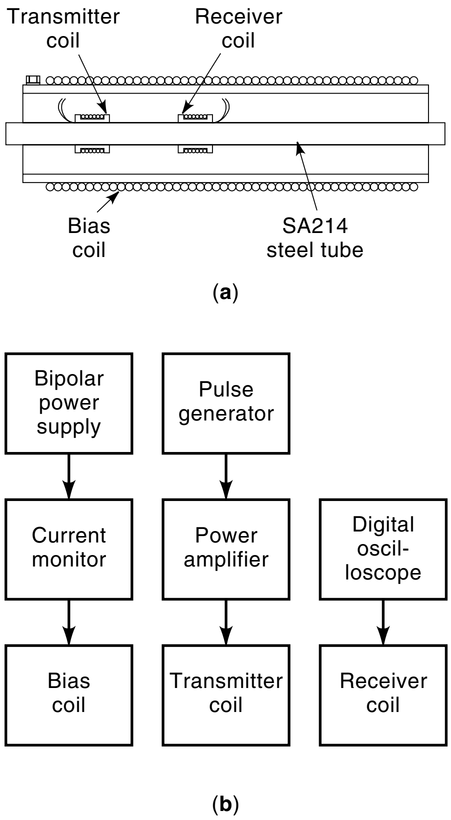

Figure 5. Magnetostrictive wave setup: (a) schematic diagram showing a steel tube surrounded by both transmitter and receiver in the axial bias field of a large dc coil; (b) block circuit diagram for bias coil, transmitter coil, and receiver coil (after Ref. 61).

Figure 6. Photograph shows an array of MsS magnetic bias field modules placed around a 406.6 mm outside diameter steel pipe. Installing an encircling ac coil on a continuous pipe is accomplished with a ribbon coil that can be strapped onto the pipe (after Ref. 56).

The MsS technique is promising. More research is needed to understand the effect of nonlinear, hysteretic magnetization and magnetostriction on the efficiency of the generation and sensing process. In addition, both defect identification and characterization need to be better addressed.

The MsS technique is similar to that of EMATS, which are used to generate elastic waves from electromagnetic waves in nonferrous media. EMATS rely on the Lorentz force to couple electromagnetic waves to the nonferrous metal; whereas the MsS approach relies on magnetostrictive coupling, which in ferromagnets is larger than Lorentz coupling. In addition, EMATS are typically meander coils, whereas the MsS geometry is cylindrical.

MAGNETIC METHODS FOR MICROSTRUCTURAL FEATURES

Microstructural NDE via Hysteresis Loop Parameters

All ferromagnetic materials exhibit hysteresis in the variation of flux density B with magnetic field H. Hysteresis means that as the field in a specimen is increased from $-H_m$ to $+H_m$, the $B(H)$ at each value of H is different from the value that exists when the field is decreased from $+H_m$ to $-H_m$. In other words, the flux density depends on the history of the H variation as well as on the value of H itself. Figure 8 shows this history dependence for a field varying between $-H_m$ and $+H_m$. The B vs H plot is known as the magnetic hysteresis loop.

In Fig. 8 are indicated various parameters associated with the hysteresis. The remanence B_r is defined as the nonzero flux density still remaining in the material when the field in the material is brought from its maximum value H_m back to zero. The coercivity H_c is the additional amount of field in the

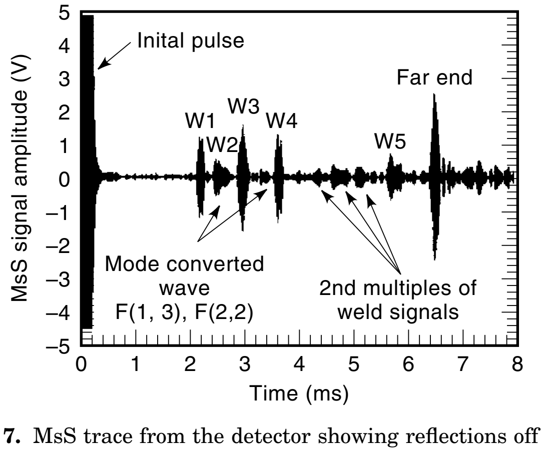

Figure 7. MsS trace from the detector showing reflections off welds, 2nd multiples of the weld signals, and the reflection from the far end of the pipe (after Ref. 53).

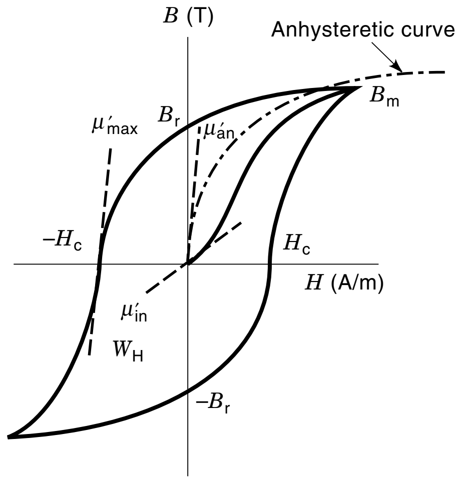

Figure 8. Hysteresis plot showing various hysteresis parameters–coercivity (H_c), remanence (B_r), maximum flux density (B_m), maximum differential permeability (μ'_{max}), initial differential permeability (μ'_{in}), the anhysteretic curve, and the initial differential anhysteretic permeability (μ'_{an}). The area inscribed by the hysteresis curve is the hysteresis loss (W_H) (after Ref. 6).

opposite direction that has to be applied before the remaining flux density in the material is finally brought back to zero. (Technically speaking, the terms remanent flux density and coercive field should be used for unsaturated loops, whose maximum flux density B_m is less than the saturation value B_s.) Note that the slope of the B–H curve, known as the differential permeability, is typically a maximum at the coercive field H_c, and so the maximum differential permeability μ'_{max} is another characteristic of the hysteresis loop. The path taken on the B–H plot when an unmagnetized specimen is brought to maximum field H_m is known as the initial magnetization curve, and the slope of the initial magnetization as the field begins to increase from $H = 0$ is known as the initial differential permeability μ'_{in}.

The area enclosed by the hysteresis loop in Fig. 8 is the hysteresis loss W_H. It has that name because the loop area is the magnetic energy that must be inputted if the material is to be completely cycled around the loop. This energy loss is associated with irreversible motion of magnetic domain walls inside the material and appears in the material as heat. The hysteresis is thus due to irreversible thermodynamic changes that develop as a result of magnetization.

Another feature, depicted in Fig. 8, is the anhysteretic curve. If a large amplitude ac field is superimposed on a constant dc bias field H and if the ac amplitude is gradually decreased, the material's flux density will tend to a value on the anhysteretic curve. By changing the bias field to H' and repeating the procedure, another point on the anhysteretic curve is obtained. At saturation, both the anhysteretic and the hysteresis curve have the same end point value. Note that the anhysteretic curve is single-valued. The slope of the anhysteretic curve at $H = 0$ is another hysteresis parameter and is called the initial differential anhysteretic permeability μ'_{an}. A paper by Sablik and Langman (62) discusses the experimental attainment of the anhysteretic curve in both the absence and the presence of mechanical stress.

All the hysteresis parameters are known to be sensitive to such factors as stress, plastic strain, grain size, heat treatment, and the presence of precipitates of a second phase, such as iron carbide in steels. Excepting stress, all of these factors refer to microstructural conditions in the material. In addition, microstructural changes can be produced by the application of stress at high temperatures; such changes, referred to as creep damage, generally involve degradation of the material so that it is more susceptible to mechanical failure such as cracking and rupture. The presence of creep damage can be sensed by characteristic magnetic property changes—that is, changes in the hysteresis parameters. Similarly, cyclic application of stress eventually results in microstructural changes that will eventually lead to mechanical failure. These microstructural changes due to cyclic stress application are known as fatigue damage, and they too are associated with characteristic magnetic property changes. Because hysteresis parameters are sensitive to microstructure and microstructural changes, the measurement of hysteresis loops for a given specimen becomes an NDE technique for characterizing microstructure. Proper systematics must be followed, so as to sort one microstructural effect from another.

One effect that must be addressed is the problem of demagnetizing effects (63) due to finite geometries and magnetic pole formation at both ends of the specimen, leading to a reduction in effective local field in the material by $-D_m M$, where D_m is known as the demagnetization factor and is dependent on sample shape. If this effect, due to finiteness and shape of the sample, is not properly addressed, apparent changes in sample magnetic properties may in fact be caused by geometrical instead of microstructural effects.

With proper care and systematics, NDE via hysteresis has had great success in evaluation of the condition of steel components. Mikheev (64) has used magnetic parameters to determine the quality of heat treatment of steels and to evaluate hardnesses of steels (65). In most cases, Mikheev used a coercivity measurement to characterize the material, and correlations were made between coercivity and chemical composition, microstructure, hardness, and heat treatment. Figure 9 is an example showing one such relationship—that H_c increases linearly with carbon content when carbon precipitates are lamellar in shape but nonlinearly when the precipitates are spheroidal (64). The effect of grain size and hardness on hysteresis parameters was studied by Kwun and Burkhardt (66), who looked at these effects in alloy steels.

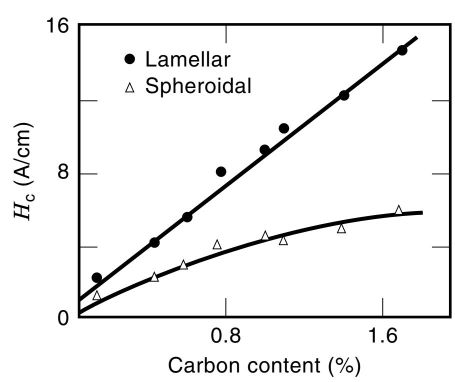

Figure 9. Variation of coercive field H_c with carbon content for lamellar and spheroidal precipitates (after Ref. 65).

Ranjan et al. (67,68) have also looked at grain size effects as well as carbon content effects in decarburized steels.

Another possible use of hysteresis parameters is in detection of creep damage (19). It is known that creep damage causes a general reduction in the values of hysteresis parameters—that is, remanence, coercivity, maximum differential permeability, and hysteresis loss (69). The reason is twofold. During creep, voids move out of the grains to the grain boundaries where they coalesce and form cavities; the cavities become magnetically polarized, creating a demagnetizing field that results in a decreased local field and decreased overall flux density and remanence (69). Also, during creep, dislocations, which normally act as domain wall pinning centers, move out of the grains to the grain boundaries, producing a reduction in coercivity (69). These effects have been modeled (19,69), using a modification of the Jiles–Atherton model of hysteresis (70). In addition, in the case where the creep damage is distributed nonuniformly, the model can be incorporated into a finite element formalism (71). This is important in the case of seam welds in steam piping because in such welds there is a greater weld width on the inside and outside of the pipe wall, but a smaller weld width in the wall interior. The stress in the pipe due to steam loading gets concentrated at the weld V inside the wall, and that is where creep damage begins. The finite element simulation shows that one can detect this creep damage, even when it is interior to the wall, by recording the induced secondary emf of a magnetic C-core detector (71).

Yet another potential use of hysteresis parameters is in NDE of fatigue damage caused by cyclic stress. In this case, the coercivity follows a very specific pattern. During the early stages of the fatigue process, the coercivity increases gradually, following a logarithmic dependence on the number N of stress cycles as: $H_c - H_{c_\eta} = b \ln N$. After a long period, a point is reached where the end failure process begins, after which the coercivity increases very rapidly (72,73). Figure 10 shows these effects. When the coercivity reaches the stage where it starts increasingly rapidly, it is time to remove the test specimen from service before it fails. Remanence shows the opposite effect and decreases linearly with $\ln N$ (73).

Another microstructural effect is plastic deformation, where slipping and movement of dislocations under large stress results in dimensional changes in a specimen after the stress is removed. The stress at which plastic deformation starts is called the yield point. Swartzendruber et al. (74) have shown that in low carbon steels, the coercivity increases as the square root of plastic strain, where strain is defined as change in length divided by length.

It is anticipated that the monitoring of hysteresis parameters will be one of the preferred future methods in monitoring creep damage, fatigue damage, and plastic deformation.

Microstructural NDE via Barkhausen Effect and Magnetoacoustic Emission

The Barkhausen effect (BE) and magnetoacoustic emission (MAE) are related effects. The BE results from irreversible step-like changes in magnetization, produced mainly by sudden movement of 180° domain walls. The discontinuous change of magnetization generates a noise-like BE voltage proportional to the time derivative of the magnetic flux into a pick-up coil placed near the material being magnetized. The

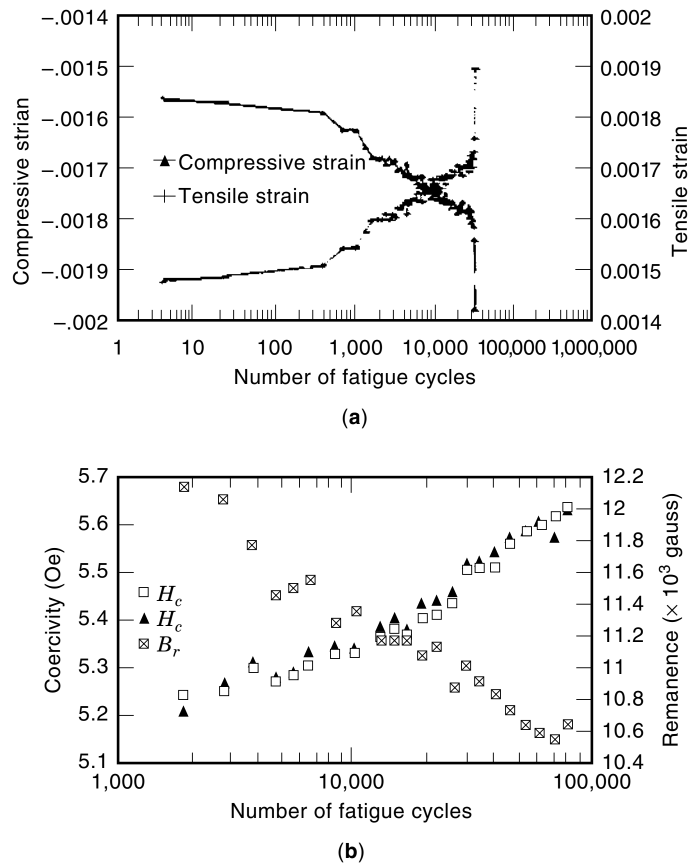

Figure 10. For A533B structural steel is depicted: (a) tensile and compressive strain as a function of number of stress cycles at fixed stress amplitude (272 MPa); (b) coercivity and remanence as a function of number of stress cycles (after Ref. 73).

MAE is caused by microscopic changes in local strain induced magnetoelastically during the discontinuous motion of non-180° walls. The acoustic waves so generated can be detected by a piezoelectric transducer bonded to the test material.

The BE is one of the most important magnetic NDE methods for investigating intrinsic properties of magnetic materials. Since its discovery in 1919 (75), the BE has been the subject of numerous investigations. The literature prior to 1975 is reviewed by Stierstadt (76) and by McClure and Schröder (77), who treat primarily the physical basis of the BE and its detection techniques. Reviews of Barkhausen applications in NDE include Refs. 2–6, 13, 78–81.

The as-received BE signal is influenced by BE electromagnetic wave signal propagation conditions in the material (82) as well by transducer properties (77,80,83). A typical BE voltage signal (U_e) induced in a pickup coil (wound on a low carbon steel bar) is shown in Fig. 11 (84). The signal was recorded during a half cycle of magnetic field H sweep, during which H increased at a constant time rate. The high frequency component (U_s) of the U_e signal, transformed to a dc-like envelope voltage signal U_b, depicts the BE intensity envelope. Its maximum usually occurs at or near coercivity field strength H_c. The MAE intensity envelope reveals mostly two maxima in the "knee" region of hysteresis. A BE and MAE measuring setup for NDE is shown schematically in Fig. 12. A biasing C-shaped magnet is cycled at low frequency (gener-

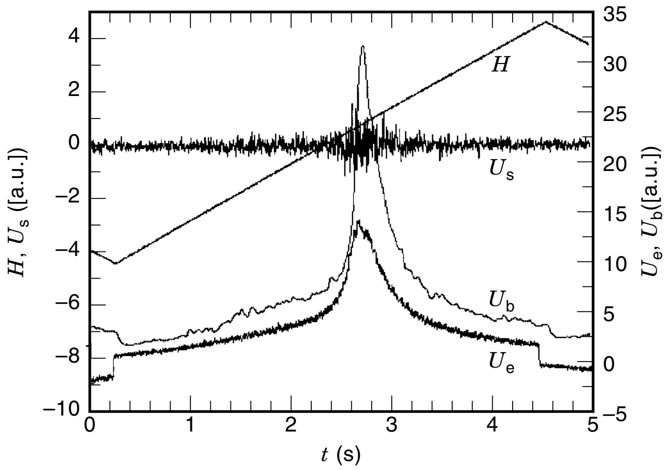

Figure 11. Schematic diagram showing time variation of the applied field H, the pickup coil voltage U_e, the BE component voltage U_s, and its envelope U_b (after Ref. 84).

ally less than 100 Hz). The BE voltage detected inductively is analyzed by a signal processor in the frequency range 1–300 kHz. The MAE probe (piezoceramic transducer, mostly resonant) provides the strain signal, which is analyzed in a range from 20 kHz to 1 MHz. It was established (85) that mostly large movement of non-180° DW or creation and annihilation of DW generates the MAE signals (86–89) while the BE signals are due to all kinds of DW movement, though mainly 180° in steel (85,90).

The various methods of BE and MAE signal processing and analysis can be separated into three main groups: (1) power spectrum analysis (77,91–93); (2) individual pulse analysis; and (3) integrated pulse analysis. Individual pulse analysis leads to pulse amplitude distribution (94), pulse amplitude and pulse duration distribution (95), and autocorrelation functions (96). The rms-like voltage (97) envelope of rectified pulses (98) and pulse count rate (67,99) signatures can be recorded as a function of applied field strength as part of individual pulse analysis. Single parameter evaluations of BE intensity such as mean value of rms (100), mean pulse amplitude (2,78), total number of pulses (101), and rectified single envelope maximum level are also used. Due to progress

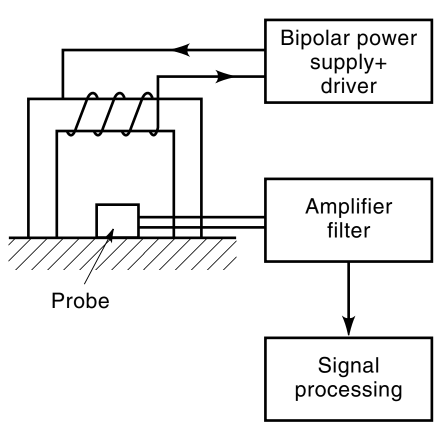

Figure 12. The BE and MAE transmitter and receiver system (after Ref. 4).

in microelectronics, BE measurement sets have been transformed from laboratory-like sets (102) to portable sets (78,81,103) and small compact (101) sets.

The BE intensity was also modeled in various ways. The rms-like parameter level was evaluated by Sakamoto et al. (104) and the power spectrum function by Alessandro et al. (92,93). Kim et al. have used a wall potential energy model for pulse amplitude (94).

The BE and MAE are dependent on the density and nature of pinning sites within the material (78). Precipitation of solute carbon as carbide is easily detected by BE analysis (67,78). Increase of particle size increases the stress field around the particle and the associated pinning effect causes a rise in BE intensity. The BE intensity maximum appears when the particle size is comparable with DW width (105). For larger particle size than DW width, new closure domains appear on the precipitate surface and magnetic structure becomes more detailed, leading to a decrease of BE pulse amplitude and BE intensity (78,97). The MAE intensity increases with increase of precipitate concentration located at grain boundaries (105).

Grain size affects the magnetic properties in two ways: first, by change of domain structure due to generation of closure domains (reverse spikes) at the grain boundaries and, second, by change of DW motion conditions because grain boundaries present obstacles to movement of DW (67). The DW moves further between pinning sites in increased size grains. An increase of grain size leads thus to an increase of rms peak level and total number of counts of the BE (67), pulse amplitude (106), pulse duration (107), and mean rms level (108). The role of grain size on BE power spectrum was discussed by Bertotti et al. in a theory in which BE is connected to the statistical properties of random local coercive fields experienced by a moving DW (109). The MAE signal intensity follows the same trend with grain size as does the BE signal (67,107).

Texture direction can be evaluated using BE due to the strong orientation effect of BE intensity (78). Komatsubara and Porteseil (110) found that the integral of BE power losses increases as a function of misorientation of grains against magnetization direction. Tiitto (108) found that BE level patterns vary systematically over a wide range of tested textures. Krause et al. (111) argued that the angular dependence of BE intensity in Si-Fe oriented steel was modulated by anisotropic internal fields that moderate 180° DW motion.

Plastic deformation changes considerably the BE intensity (78). The zero-stress BE intensity decreases within small tensile plastic strain (5,78,91,112,113) and increases for compressive plastic strain (5,13) indicating “compressive-like” and “tensile-like” residual stress, respectively, due to plastic strain. The BE and MAE intensities are reduced during annealing of plastically deformed steel due to dislocation density decrease (112).

The BE intensity is correlated with hardness level (4,5). A decrease of hardness of hardened parts is accompanied by an increase of BE intensity (5). Two frequency bands of BE signal filtering were used in order to evaluate surface hardening depth (4,114).

New approaches to NDE of microstructure are possible using MAE, in which Barkhausen pulses due to non- 180° DW jumps are detected during sample loading within the elastic range of stress (6,78,79,89,95,99,115). A distribution function of internal stress at microstructural defects is obtainable directly from strain dependence of the MAE intensity (99,116).

The BE and MAE are used to analyze microstructure change due to various thermal treatments (78,97,113,117). A decrease of dislocation density with tempering time was found to be correlated with different BE and MAE dependences on time (117). Buttle et al. tested the result of heat treatment of strained iron and have proposed simultaneous measurement of BE and MAE for NDE characterization of materials microstructure (112).

Structural degradation of industrial materials due to fatigue or creep is an important NDE application of the Barkhausen effect (2,11). Sundstrom and Torronen report preliminary results indicating that BE can be used for in-service inspection of high-temperature pipelines of ferritic materials used in power stations (2). The as-observed decrease of the BE intensity in the overheated areas of tested tubes was well correlated with reduction of hardness level. Lamontanara et al. have tested the influence of cycling load and plastic deformation on BE properties in boiler tubes correlating change of BE parameters with fatigue damage (11). Monotonic decrease of BE intensity was observed for power station tubes as a function of their exploitation time (118). Similar decrease in Barkhausen signal due to fatigue was found by Chen et al. (119).

Other applications of BE include grinding, shot-peening, and crack propagation. Grinding operations provide microstructure changes which can be detected by means of BE inspection (5,120). Tiitto looked at increase of BE intensity as an indication of grinding burns on a camshaft valve lobe (5) and ball bearing surface (108). Shot peening as a surface treatment for extending fatigue life can be controlled by means of BE inspection (108,121). McClure et al. (122) and Battacharya and Schröder (123) used both BE and MAE to detect discontinuous changes in magnetization of ferromagnets caused by fatigue crack propagation.

The BE and MAE methods have been clearly established as viable NDE techniques for NDE microstructural changes evaluation. The physical mechanisms for microstructural influences on the Barkhausen effect need to be further elucidated. Also, measurement conditions and signal processing should be delineated carefully so as to establish NDE procedure standards.

MAGNETIC NDE OF RESIDUAL STRESS

Inhomogeneous heat treatment due to welding and inhomogeneous plastic deformation during fabrication can leave strong residual stresses inside steel components (12). These stresses affect component service life because they can add to applied loads causing fatigue and failure. The residual stresses might also be beneficial. For example, railroad wheels have compressive residual stress built into the wheel rims to inhibit crack formation. Through braking and general use, the compressive stress in the wheel rim can change to tensile stress, which can cause cracks in the rim to widen (16,124). For these and many reasons, an NDE method for measuring stress is sought.

Of the NDE methods for measuring residual stress (125), none currently gives a complete map of stress field inside each component. In this section, we discuss magnetic properties that correlate with stress and note how they are used for NDE of residual stress.

Using Hysteresis Parameters for Residual Stress NDE

The effect of stress on magnetization has been studied for many years (126–137). The vast majority of work has been one-dimensional (i.e., stress axis, applied magnetic field, and magnetization all collinear along the same axis). Recently, noncoaxial stress, field, and magnetization has been investigated (137,138). In addition, there have been magnetic studies where the stresses are biaxial, that is, two stresses act independently along two perpendicular axes (18,139–146).

Two major types of magnetic processes have been studied—σH processes and $H\sigma$ processes. In σH processes, stress (σ) is first applied and then H is varied while stress is kept constant. A typical σH process is a magnetic hysteresis loop taken at constant stress. This would be the way NDE hysteresis measurements would be conducted. In the $H\sigma$ process, the field is first set at a constant nonzero value, and then magnetization varies as applied stress is varied (128,135). Discussion here is restricted to σH processes, as they apply to NDE measurements.

Three major model types account for hysteresis in materials undergoing the σH process. First, a macroscopic model has been developed by Sablik and Jiles (and others) for polycrystalline ferromagnets (17,132,136,137,147). Second, a micromagnetic model, taking into account domain wall types, has been developed for crystals and polycrystals by Schneider et al. (135), Schneider and Richardson (140), and Schneider and Charlesworth (148). Third, another micromagnetic model, using an energy formulation and a statistical formulation for the domains, is due to Hauser and Fulmek (134) and Hauser (149,150), who applied it mostly to crystalline and grain-oriented Fe(Si) alloy steel. In addition, Garshelis and Fiegel have proposed a simple nonhysteretic model for stress effects on magnetic properties (151). Early models were also given by Brown (152,153), and Smith and Birchak (154). A recent model relating stress to magnetic properties in thin magnetic films has been developed by Callegaro and Puppin (155).

The effects of stress on ferromagnetic materials is complicated, as several factors must be considered. For instance, it must be known whether the stress is within the elastic range of the material or whether it is plastically deforming the material. Also, one must know something about the nature of the magnetostriction—whether, for example, it is positive or negative.

Magnetostriction refers to the change in dimensions of ferromagnetic materials as they are magnetized. The relative change in dimensions is quite small ($\sim 10^{-5}$ or 10^{-6}) for most ferromagnetic materials and depends on the strength and orientation of the applied field. A material with positive magnetostriction increases in length along the magnetization direction. Conversely, a material with negative magnetostriction decreases in length along the magnetization direction.

A tensile stress, applied to a material with positive magnetostriction, will generally increase the magnetic induction B. The stress produces an effective magnetic field that acts in conjunction with the applied magnetic field and in effect adds to it. A compressive stress, applied to a material with positive magnetostriction, generally decreases magnetic induction B.

In this case, the stress produces an effective magnetic field that opposes the applied magnetic field.

Many ferrous alloys have a mixed type of magnetostriction depending on the applied magnetic field and stress. Iron, under zero stress, has a positive magnetostriction up to about 250 Oe (20 kA/m); above this, it has a negative magnetostriction (13). In alloys, the field that produces a change in sign of the magnetostriction will be different depending on stress and material composition. Nickel has a negative magnetostriction (126); this is true also of some ferrites (156).

In low magnetic fields and under tensile stress in the elastic range, ferrous alloys with positive magnetostriction show increased magnetic induction with increased applied stress. The effect is nearly linear until a magnitude of stress is reached at which the induction reaches a maximum, after which for higher stresses, induction is smaller. This appearance of this maximum under tensile stress is called the Villari effect (137,157). An explanation often advanced for this effect is a change in sign of the magnetostriction with increased stress (13). More exactly, it would be a change in sign of the derivative of the bulk magnetostriction with respect to the bulk magnetization ($d\lambda/dM$), because the stress effective field H_σ is predicted to be proportional to $d\lambda/dM$ (17,136,137,158). Other explanations have been also given for the Villari effect (135). One of these is that as tensile stress is increased, the domains antiparallel to the magnetization tend to shrink and disappear, with the result that the magnetostriction tends not to change as much under tensile stress, leading to a shrinking $d\lambda/dM$ which tends to produce a maximum in the magnetic induction (147). Under compression, a stress-caused demagnetization term $-D_\sigma M$ comes about because compression produces spatial divergence of magnetization near grain boundaries (viz., $|\nabla \cdot \boldsymbol{M}| \neq 0$), which in turn results in magnetic poles at the grain boundaries, producing a demagnetization field that subtracts from the magnetic induction (147). The effect of the demagnetization term is so strong for applied compressive stresses that it counteracts the effect of reduction in $d\lambda/dM$. For this reason, the Villari extremum is not seen under compressive stress. The behavior is thus asymmetric (147). The fact that a maximum appears in the magnetic induction under tensile stress and coaxial field H complicates NDE measurement of stress.

Even more complications come about when stress and field are noncoaxial (i.e., stress axis and field are at an angle θ with respect to each other). Generally, in an isotropic or polycrystalline ferromagnetic material, an angle θ can be found for which stress causes no change in magnetic properties when stress and field are noncoaxial (137,138). If the field is *perpendicular* to the stress axis, then for σH processes, increased stress under tension produces *decreased* magnetic induction for each value of H, and vice versa for compression (130,131,137,138). Furthermore, the Villari extremum shifts to negative (i.e., compressive) stresses (137). Because of all these extra complications, an NDE measurement of stress must be carefully designed.

The process is simplified if the direction of the stress axis is known (for, in that case, the magnetic field can be applied parallel to the stress axis) and a low enough field can be applied that the magnetic properties vary canonically with stress. In such a situation, for positive magnetostriction, the remanence B_r should be increased linearly with increased tensile stress and decreased linearly with increased compressive stress; similarly, for B_{max} and M_{max} (136). The coercivity, on the other hand, is decreased with increased compressive stress (137).

In the small field–small stress range, one can obtain the stress from the hysteresis parameters, provided one calibrates the parameters for the unstressed material and knows the stress axis direction. This works well if there is little variation in properties from sample to sample (as often happens for commercial steels). If the stress axis direction is unknown, the angular variation of the magnetic properties can be used to determine the stress axis direction (137).

Measuring stress using hysteresis parameters is a *bulk* stress measurement, usually with an error that is $\pm$ 5–10% of yield point stress. The bulk measurement is unlike X-ray and Barkhausen noise measurements, which yield only *surface* stress (2,5).

Generally speaking, hysteresis loops, true to the specimen, are measured when a cylindrical specimen is wrapped inside an excitation coil, with a secondary coil also wrapped around the specimen in the center of excitation coil, and with a Hall probe positioned next to the specimen surface to measure H. This approach, called the permeameter approach, most assuredly measures the intrinsic magnetic properties of the specimen. Alternating current I is applied to the excitation coil and the resulting alternating magnetic induction B in the specimen induces a voltage in the secondary coil, the signal from which is then phase-adjusted to be in synchronization with the Hall voltage detected, so that a hysteresis loop can be generated. Quasi-dc properties can be determined by using low frequencies of the order 0.5 Hz to 2 Hz.

An NDE field probe, in most cases, must be small and portable, and so, out in the field, the probe is usually a C-core, that is, an electromagnet, in the shape of either a circular or squared-off C, for which the pole pieces are designed to be flush with the sample. The hysteresis loop, measured with a secondary coil wrapped around one of the pole pieces close to the specimen, is not the true hysteresis loop of the specimen; however, that does not matter if stress is being measured because the loop that is measured is influenced by the stress acting on the specimen and will vary proportionally to the true stress-influenced hysteresis loop of the specimen. Hence, the variations of the hysteresis loop obtained with a C-core can still be calibrated with the stress, provided the C-core is always flush against the specimen. If there is a variable air space (liftoff) between the C-core and the specimen, there will be flux leakage and the method will not be reliable. Thus, NDE of stress (usually with a C-core) must also contend with this liftoff issue (159).

There are many papers that discuss NDE of stress by using one or more of the hysteresis parameters. The earliest seems to be that of Ershov and Shel (160), who used magnetic permeability to measure tensile stress in steel with the magnetic field both perpendicular and parallel to the stress axis. Abiku and Cullity (161), and later Abiku (162), used permeability to measure stress in steel and nickel. Musikhin et al. (163) used the coercive field as an NDE indicator of stress. Devine (164) described the detection of stress in railroad steels via many magnetic property measurements, using remanence, coercivity, maximum differential permeability, and hysteresis loss. For the case of biaxial stress, a method has been suggested by Sablik (18) for measuring the difference in the biaxial stresses using hysteresis parameter measurements for cases where the parameters are measured first with the magnetic field parallel to one of the stress axes and then perpendicular to it. For an absolute measurement of the stresses along both axes, a technique with the magnetic field perpendicular to the biaxial stress plane is discussed (146).

Nonlinear Harmonic Method (NLH)

The magnetic induction B (magnetic flux density) of a ferromagnetic material, when subjected to a sinusoidally varying field H, is not sinusoidal but distorted. This is due to nonlinear, hysteretic variation of the magnetic induction with field H. Figure 13 illustrates how a sinusoidal H produces a nonsinusoidal induction B because of magnetic hysteresis (9).

The distorted waveform of B contains odd harmonics. The reason that only odd harmonics of B are present is because B must satisfy (165)

$$B(t \pm (T/2)) = -B(t) \tag{2}$$

because, as seen in Fig. 13, the waveform of B repeats itself over the second half of the cycle but is negative. In Eq. (2), T is the period of the waveform and is equal to $T = 1/f = 2\pi/\omega$, where ω is angular frequency and f is frequency. Each harmonic has a period $\tau_n = T/n$. Thus, when $n = 2$, $B(t \pm (T/2)) = B(t \pm \tau_n) = B(t)$ is not Eq. (2); when $n = 3$, $B(t \pm (T/2)) = B(t \pm (3\tau_n)/2)) = -B(t)$. It is seen that only odd n can satisfy Eq. (2).

Because stresses influence the magnetic hysteresis, it follows that the harmonic content of the magnetic induction is also sensitive to the stress. With NLH, these harmonic frequencies are detected, and their amplitudes are related to the state of stress in the material (166,167).

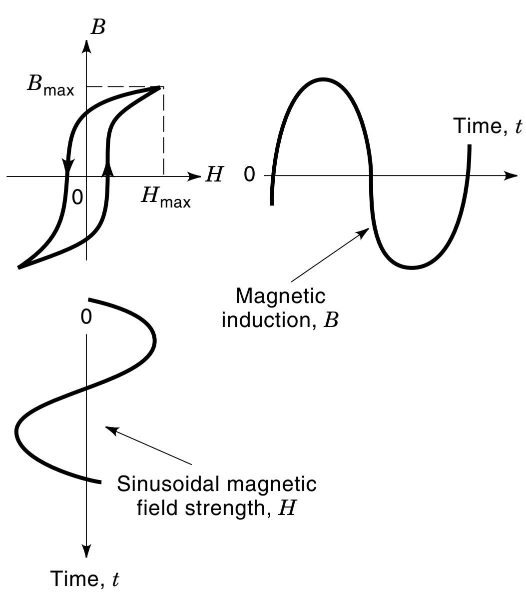

Figure 13. Distortion of the magnetic induction B caused by nonlinearity in hysteresis. The curve for B consists of a fundamental and higher order odd harmonics (after Ref. 9).

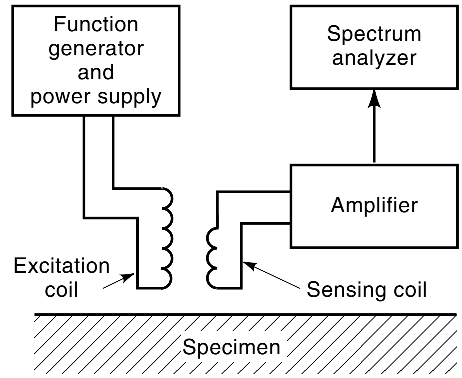

Figure 14. Block diagram illustrating nonlinear harmonics instrumentation (after Ref. 9).

The NLH instrumentation is shown schematically in Fig. 14 (9). The magnetic field H is applied to the specimen with an excitation coil and the resulting magnetic induction measured with a sensing coil. A C-core setup or wrapped coil about a cylindrical specimen can be used. The sinusoidal excitation current is supplied by a function generator (or oscillator) and power amplifier. The induced voltage in the sensing coil is amplified and, via the use of filters, the harmonic signals are separated from each other, amplified, and analyzed. Typically, the third, fifth and possibly seventh harmonic signal can be displayed. However, only the third harmonic signal is used for stress determination, because that usually has the largest amplitude.

The harmonic amplitudes depend not only on stress, but also on relative orientation of stress and field. When positive magnetostriction applies, the harmonic amplitude increases with tension when stress and field axes are parallel and decreases when they are perpendicular.

The NHL technique senses stresses with sensing depth near the ac skin depth. Because skin depth is a function of frequency, the sensing depth can be varied with the frequency. By using quasi dc frequencies, a near bulk measurement is also possible.

The NLH measurements are sensitive to factors unrelated to stress, such as microstructure, heat treatment, and material variables. If a C-core is used, then the possibility of an air space between probe and sample can cause problems, particularly on a curved surface such as a pipe. All of these other factors must be considered when doing the NLH measurement.

This technique is usually effective to a range of stress of up to about 50% of the yield stress, and the accuracy of the technique is about ± 35 MPa (± 5 kpsi). At stress levels of higher than 50% of yield stress, the NHL response tends to saturate. With this technique, stress can be measured while scanning at high speed [~10 m/s, (or approximately 30 ft/s)] (167). This technique thus has a potential for rapidly surveying stress states in pipelines or continuously welded rail (167,168). A simple model for simulating NLH analysis of stress may be found in Ref. 158.

Stress Induced Magnetic Anisotropy (SMA)

In the absence of stress, a polycrystalline ferromagnetic material without texture will have isotropic magnetic properties

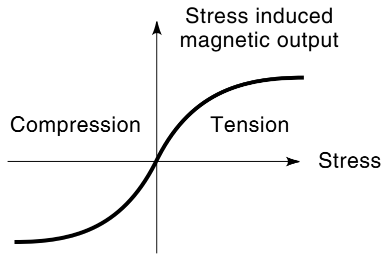

Figure 15. B_n/B_p ratio against stress, showing continuous change from compressive to tensile loads (after Ref. 20).

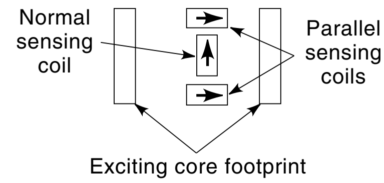

Figure 16. Concept diagram for Langman's SMA measurement (after Ref. 20).

independent of the direction of measurement. In the presence of stress, this is no longer true, and the material becomes magnetically anisotropic, an effect known as stress-induced magnetic anisotropy (SMA) (141). For mild steel, the peak magnetic flux density ratio between directions parallel and perpendicular to the stress axis can be as high as 5 (130). As mentioned earlier, the physics for understanding the difference in magnetic response in different directions has been developed by Sablik et al. (137). Although any magnetic method for measuring stress could be considered an SMA technique, the term is usually reserved for techniques that simultaneously measure magnetic properties in perpendicular directions.

In a series of papers (16,130,139,169,170) Langman describes an SMA technique based on measuring the angle between magnetic field intensity H and magnetic flux density B. Magnetic permeability μ, a scalar in an isotropic ferromagnetic material but dependent on the magnitude of H, becomes a tensor in the presence of stress and $\boldsymbol{H}$ and $\boldsymbol{B}$ vectors no longer are parallel in the general case. $\boldsymbol{B}$ will be canted with respect to $\boldsymbol{H}$. Langman's SMA technique detects the induced flux normal to the applied field, which in a magnetically isotropic material would be zero. For analysis purposes, Langman considers the ratio between the flux density component (B_n) normal to the applied field and the flux density component (B_p) parallel to it (viz., B_n/B_p). In Fig. 15, it is shown how the ratio B_n/B_p changes continuously as the stress changes from compression (negative stress) to tension (positive stress). For biaxial stresses, this ratio is proportional to the algebraic difference of the two biaxial stresses (viz., $B_n/B_p = f(\sigma_1 - \sigma_2)$, where σ_1 is the stress along one axis and σ_2 is the stress along the other). A plot similar to that of Fig. 15 is found, where now the abscissa is $\sigma_1 - \sigma_2$. Note that the behavior seen in Fig. 15 is linear at low values of stress, becoming nonlinear at about 1/3 of the yield strength, after which the response shows a tendency to saturation. A similar behavior was encountered also for NLH in the last section. An error margin reported for this type of measurement is 20 MPa in the difference between principal stresses and roughly 5° in their direction, when the stresses are biaxial (20).

Figure 16 shows a concept diagram for Langman's SMA probe. The pole pieces of the core of the magnetizing coil induce a strong field in one direction. A modulation frequency of between 30 and 80 Hz is used, which is equivalent to an inspection depth of about 0.5 mm in mild steel. Two air-cored pickup coils parallel to and close to specimen's surface $\boldsymbol{H}$ are placed on either side of a third air-cored pickup coil, which is perpendicular to exciting field $\boldsymbol{H}$. The outputs of these coils are translated into the ratio B_n/B_p. The whole rig is rotated obtaining a sinusoidal output at twice the rotation rate with extremes in value at 45° to the principal stress axes, in the case of biaxial stress. By pinpointing the directions in which these extremes occur, one can locate the stress axes. Typical excitation fields are of the order of several hundred A/m (139). Difficulties are encountered when the inspection surface is not flat.

Another type of SMA probe, used in Japan, is known as a magnetic anisotropy sensor (MAS) (171–173). It differs from Langman's probe in that it consists of two perpendicularly positioned magnetic cores instead of one magnetic core and three air cores. Figure 17 shows the basic construction. In the case of the Kashiwaya MAS probe (171), the detector core has an air space (liftoff) between its pole pieces and the specimen. The finite air space makes the detector less sensitive to variations in liftoff. In the case of the Wakiwaka et al. (172) and Kishimoto et al. (173) probe, neither exciter core nor detector core has any built-in liftoff. These authors provide an analysis, which considers the reluctances of flux paths and analyzes the result from the point of view of an equivalent magnetic circuit. Again, the MAS output voltage is largest at 45° with respect to the principal stress axes, having a cloverleaf representation on a polar plot (see Fig. 18). Note that the cloverleaf increases in size as frequency is increased. Figure 19 shows a plot of the MAS output voltage vs stress, for relatively low stress values, for which the response is fairly linear.

Most applications of SMA (or MAS) have been in mild steel for the railroad industry. Measurements of railroad rail longitudinal stresses were performed in Japan (171). Stress differ-

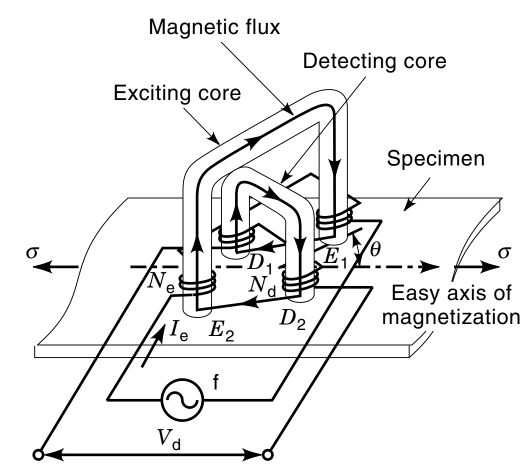

Figure 17. Basic construction of the MAS sensor (after Ref. 173).

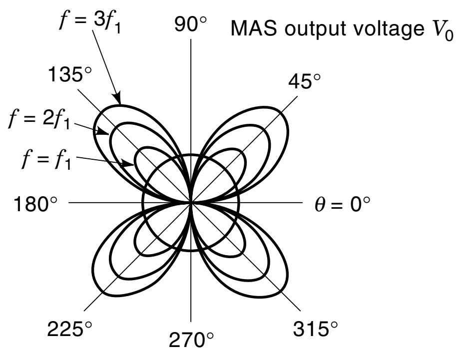

Figure 18. Calculated frequency dependence of magnetic anisotropy signal patterns (after Ref. 173).

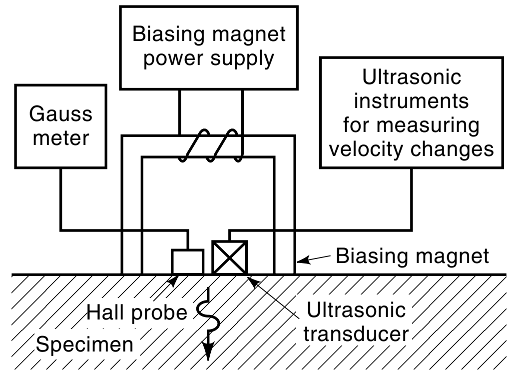

Figure 20. Block diagram of instrumentation for measuring MIVC (after Ref. 9).

ences due to day-night heating and cooling of railroad rail were measured. A three-point probe (174) for curved surfaces was used for biaxial stress measurement in a railroad car axle. Langman used his SMA technique to do field studies of stresses in railway wheels (16).

Magnetically Induced Velocity Changes (MIVC) for Ultrasonic Waves

In MIVC, the dependence of the elastic moduli on the magnetization is exploited as an NDE technique. One utilizes this dependence by passing ultrasonic waves through the magnetized material and measuring change in transit time between when the material is magnetized and when it is not. The elastic moduli are affected not only by a magnetic field but also by stress (which changes the magnetization). Thus, stress changes the MIVC. Indeed, the MIVC for ultrasonic waves is not only dependent on stress but also on the angle between the stress direction and the direction of the applied magnetic field (175,176). The characteristic stress dependence of the MIVC is used for stress determination (9,14,175–178).

Figure 20 shows a diagram of the instrumentation for measuring MIVC. An electromagnet supplies a biasing magnetic field H to the specimen. The applied field H is measured with a Hall probe. A transducer transmits ultrasonic waves to the specimen and detects signals reflected from the back of the specimen. For surface waves, separate transmitting and receiving transducers are used. The shift in arrival time of the received ultrasonic wave, caused by velocity change due to field and stress, is measured using the phase comparison technique (175).

Typical plots are seen in Fig. 21 for longitudinal MIVC = $\Delta v/v_0$ against applied field H, where v_0 is the velocity in the absence of H, and $\Delta v = v - v_0$ is the change in velocity due

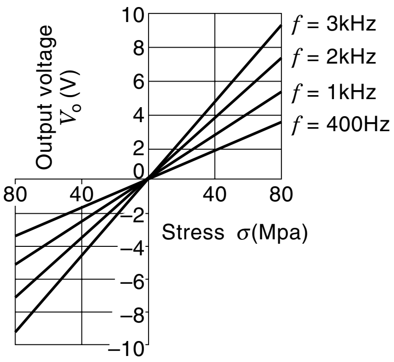

Figure 19. Calculations of MAS output voltage V_0 vs stress σ for low-carbon steel (after Ref. 173).

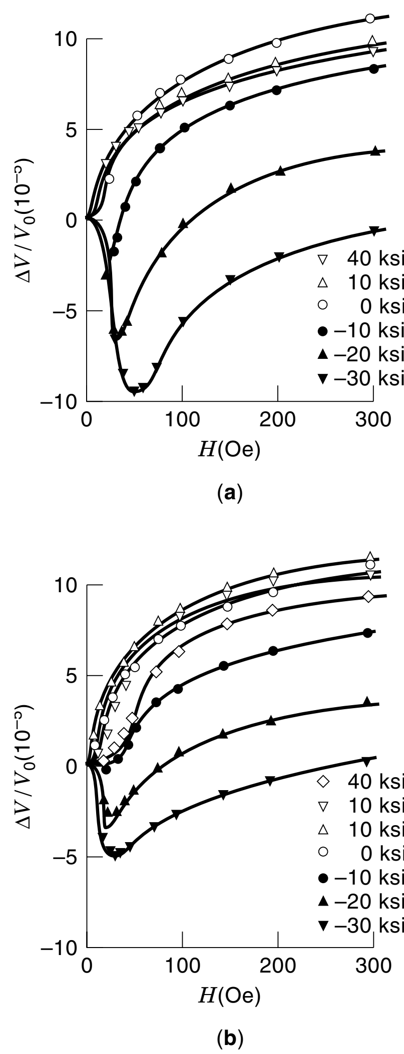

Figure 21. Longitudinal wave velocity vs magnetic field H for various stress levels in A-514C steel with H (a) parallel and (b) perpendicular to the stress axis (after Ref. 177).

to the presence of H. Figure 21(a) applies when H is parallel to the stress axis for positive magnetostriction materials. It is noted in Fig. 21(a) that under uniaxial tension ($\sigma > 0$), the MIVC is decreased from its $\sigma = 0$ value but stays positive and gets larger with increased H, ultimately saturating. Compression ($\sigma < 0$) results in a reduction of the MIVC from its $\sigma = 0$ value, but with the MIVC starting out negative, reaching a minimum, and then increasing, finally reaching positive values at large H. The more negative the compression, the deeper the minimum. For $\boldsymbol{H}$ perpendicular to the stress axis [Fig. 21(b)], the MIVC behavior under compression is similar but, under tension, the MIVC is larger at small tensions, and smaller at large tensions than the case for $\sigma = 0$.

The detailed dependence of the MIVC on stress varies depending on the sign of stress (tensile or compressive, i.e., positive or negative), the stress type (uniaxial or biaxial), the angle between the stress axis and the applied magnetic field, the wave mode used (shear, longitudinal, or surface), and material grades. Generally, NDE studies (14,177,178) have shown that an unknown stress in the material can be characterized (magnitude, direction and sign) utilizing the known stress dependences of the MIVC. The MIVC has been used to measure residual welding stresses (177), residual hoop stresses in railroad wheels (178), and through-wall detection of biaxial stresses in operating pipelines (14). In the case of biaxial stress, it is found that the MIVC works better for compression than for tension (145). Thus, MIVC would complement other measurements of biaxial stress that work between under tension than compression (146).

The MIVC technique can be used to measure bulk or surface stresses by applying bulk (shear or longitudinal) or surface ultrasonic waves. A measurement can be made in a few seconds. However, because MIVC depends on material, reference calibration curves need to be established for the material. The technique has the advantage of being insensitive to variations in texture and composition of nominally the same material. The accuracy in stress measurement is similar to that of other methods (± 35 MPa or ± 5 kpsi). One disadvantage of the technique is that a relatively large electromagnet is needed to magnetize the part under investigation, which may be cumbersome in practical application. Also, because of the difficulty in magnetizing parts of complex geometry, the application of the technique is limited to relatively simple geometries.

Barkhausen Effect and Magnetoacoustic Emission for Residual Stress NDE

The Barkhausen effect (BE) and magnetoacoustic emission (MAE) are sensitive to stress, making them important, truly nondestructive, portable and fast alternative NDE tools for residual stress measurements. The origin of stress dependence lies in the interaction between strain and local magnetization. Under uniaxial stress, the results consistently show that tension increases, while compression decreases, the BE intensity for positive magnetostriction materials (77,78). Shibata and Ono (179) and Burkhardt et al. (180), in early works on MAE, revealed that MAE intensity decreases under *both* tensile and compressive stress. Rautioho et al. tested the impact of microstructure on the stress dependence of BE (181). Examples of studies of uniaxial load on BE and MAE intensity are reported in Refs. 182–185.

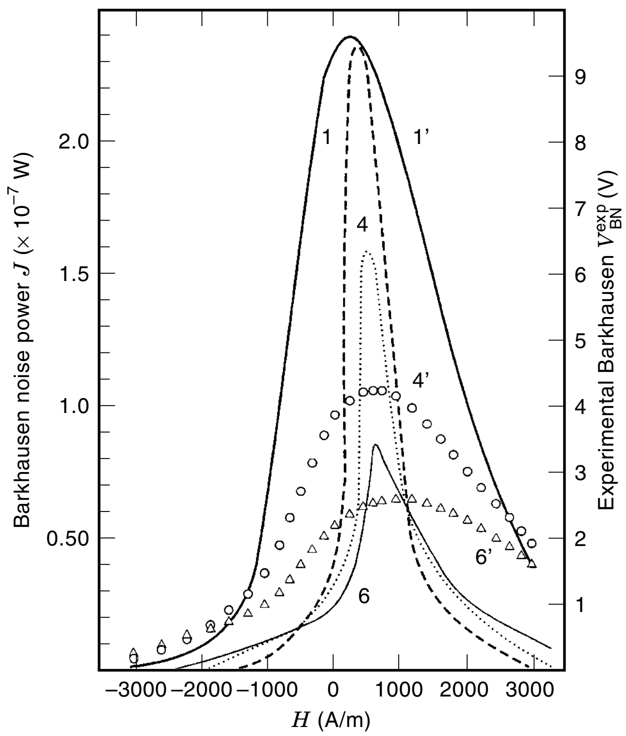

Figure 22. Measured BE intensity (1,4,6) and computed BE power (1′,4′,6′) as a function of H with stress (in MPa) acting as: (1) + 114, (4) −37, (6) − 162 (after Ref. 187).

The impact of uniaxial stress on BE intensity was modeled by Tiitto (5,108), utilizing statistical consideration of the domain magnetization vector distribution under load. Sablik (186) applied the magnetomechanical hysteresis model of Sablik and Jiles (136) to compute the normalized BE signal from the derivative of the irreversible component of magnetization, utilizing the BE power spectrum model of Allesandro et al. (92). Sablik's model was recently applied to fit results of BE measurements (187). Figure 22 shows the result of comparison of experimental and computed BE envelopes for uniaxial load of low carbon steel.

The BE intensity depends on the angle between uniaxial load and magnetization direction. When stress and field directions are parallel, tension causes an increase in BE intensity while compression causes a decrease; when the field is perpendicular to the stress axis, the effects of stress are reversed (78). The angular dependence of BE was evaluated by Kwun (138) and by Sablik (17). Stress dependence of BE intensity has been applied to load sensor design (81,188).

With biaxial load, the transverse tensile stress mostly decreases and compressive stress increases the BE intensity (78). In practice, biaxial calibration of BE intensity as a function of applied strains utilizes cross-shaped samples and four bending point modes of load (108,189).

Evaluation of stress due to welding is an example of BE and MAE industrial application (101,108,190–192). The BE intensity measurements are performed at a given point in two directions: along and across the weld seam, assuming that one of these directions is parallel to the main stress axis. Enhancement of stress resolution was achieved using the number of BE pulses as the BE intensity parameter (193). Figure

23 presents a residual stress distribution in a direction perpendicular to weld seam line, evaluated via the number of BE pulses. The BE results for weld stress analysis have been confirmed by NDE X-ray analysis as well by the hole drilling method (108,193). Stress dependence of BE signal in pipeline steels were tested by Jagadish et al., using rms signal, pulse height distribution and power spectra (194). Special application of BE stress evaluation to roll surface inspection is reported in Ref. 78.

Since the discovery that the Barkhausen effect can be used for NDE of stress (195), the Barkhausen effect has become one of the usual techniques for NDE of residual stress (100,101) and commercial apparatus sets are available for this usage. The technique has a drawback in that the measured stress distributions are near the surface. The high-frequency electromagnetic signals generated by domain wall motion in the interior of the specimen are quickly attenuated by eddy currents before they reach the surface. The effective depth for stress detection is about 0.5 mm. When bulk stress evaluation is needed, another NDE method might be better.

The MAE can in principle be used for bulk residual stress measurement because the acoustic waves generated by domain wall motion do not attenuate as rapidly as electromagnetic BE waves. However, there are problems. First, the MAE transducer used for detection requires a couplant to the specimen, whereas the BE technique is noncontacting. There are also signals coming from surface-reflected waves that must be separated from signals coming directly from moving domain walls. Also, MAE intensity is not a monotonic function of strain or stress in the near stress region [In fact, it peaks at zero stress (179,180)]. More research is needed on MAE.

Other Magnetic Methods for Residual Stress NDE

Another NDE method for stress evaluation is the incremental permeability technique (4). This refers to a time varying change of the magnetic field superimposed on bias field H. In effect, the flux density is varied along a minor loop originating

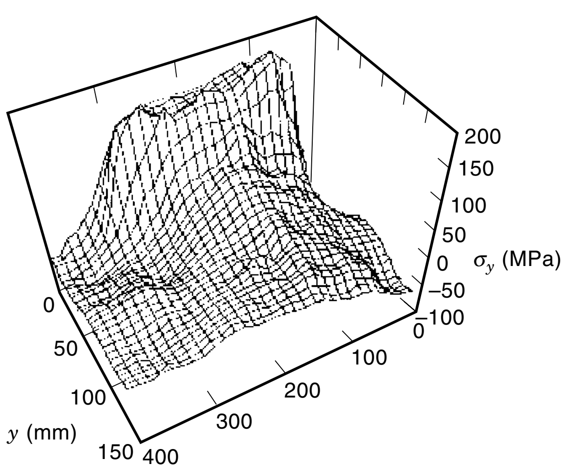

Figure 23. A 3D presentation of the residual stress over the welded plate in a direction perpendicular to the weld seam, as evaluated from the BE measurements (after Ref. 189).

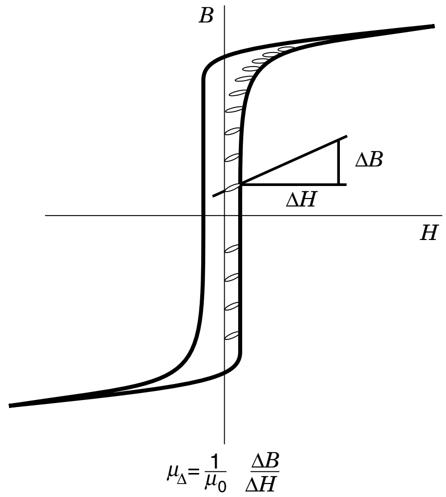

Figure 24. Plot showing how the incremental permeability is obtained from the average slope of a minor loop (after Ref. 4).

at a field point H on a major hysteresis loop. Figure 24 shows this type of variation, starting at many different points on the major loop (4). Each of the different minor loops has an average slope $\Delta B/\Delta H$, which depends on the stress that is acting. The slope is called the incremental permeability. Division by μ_0 produces the incremental "relative" permeability. Incremental permeability is dependent not only on stress but also on microstructure, and has been used for magnetic NDE assessment of hardness (196). The incremental permeability is called "reversible" permeability (197) because variation of the field along the minor loop is small enough that the change in magnetization is due to domain wall bowing and bending, which is a reversible process. Imposition of a radio frequency time-varying signal on the bias field H yields essentially the same technique, but when rf is used, it is called *magabsorption* (8,197). In that case, the time variation of the B–H slope (permeability) is monitored on an oscilloscope, and the maximum slope (instead of the average slope) is correlated with stress. A magnetomechanical hysteresis model has been given for the magabsorption (197).

Yet another variant involving the use of permeability for stress measurement is the differential effective permeability (DEP) technique (15). In this case, the initial permeability is effectively used to measure stress. A small-amplitude time-varying $H(t)$ and $H = 0$ produces what is known as a Rayleigh loop. The Rayleigh loop effectively corresponds to a minor loop in the incremental permeability technique, except that it is centered about $H = 0$. The slope of the loop depends on stress. The DEP technique has been used for biaxial stress management (15).

Another approach, which has not yet been fully implemented, is to exploit the dependence of the magnetostriction on stress. Although the dependence of magnetostriction on stress tends to be more nonlinear than many of the other properties, magnetostriction offers the possibility of additional NDE characterization in a multiparameter investigation (102).

PROMISING NEW MAGNETIC TECHNIQUES

One potentially new NDE technique is magnetic force microscropy (MFM) (198). The MFM involves sensitively mapping

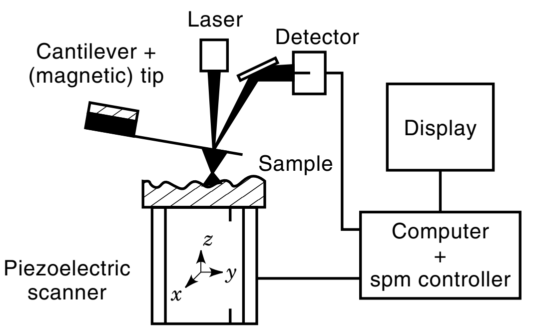

Figure 25. Schematic for a scanning probe magnetic force microscope (after Ref. 198).

surface magnetic fields (and thus surface topography) over a 20 μm size area (for example). The scanning probe has a sharp point and is mounted on a weak cantilever. (See Fig. 25.) Magnetic interactions between the scanning tip and the specimen cause the cantilever to deflect. This deflection is detected by reflecting a laser beam off the back of the cantilever into a position-sensitive photodiode. A map of the cantilever deflection obtained from the photo output gives an image of the surface topography. Because the instrumentation can be transportable, MFM is promising as an NDE tool for determining surface microstructure. A less sensitive form of MFM should help in measuring magnetic leakage fields and in locating cracks, corrosion pits, and other microscopic flaws. Two drawbacks remain: (1) frequent replacement of the tip, which wears easily; and (2) the necessity for calibration of the tip at the start and end of each daily usage. Another issue concerns the need for surface preparation. Also, MFM and related techniques at present are very costly, and interpretation is still currently difficult.

A second technique that shows promise for NDE involves use of commercial high-T_c SQUIDs. The high-T_c superconducting quantum interference device (SQUID) needs liquid nitrogen as a coolant (rather than liquid helium). This means that it could be used as a portable field device as liquid nitrogen is fairly cheap. Because a SQUID can measure magnetic flux densities very precisely (199), it could be used with nonferrous metals as a magentic leakage field detector in the case of the electric current perturbation technique (199). Another use would be detection of fatigue damage in nonferromagnetic stainless steels (200), where fatigue causes formation of ferritic steel regions, which are ferromagnetic and enhance the overall magnetic field detected for the stainless steel.

BIBLIOGRAPHY

1. F. W. Dunn, Magnetic particle inspection fundamentals, *Mater. Eval.,* **35**: 42–47, Dec. 1977.
2. O. Sundstrom and K. Torronen, The use of Barkhausen noise analysis in nondestructive testing, *Mater. Eval.,* **37**: 51–56, Feb. 1979.
3. J. F. Bussiere, On-line measurement of the microstructure and mechanical properties of steel, *Mater. Eval.,* **44**: 560–567, Apr. 1986.
4. P. Holler, Nondestructive analysis of structure and stresses by ultrasonic and micromagnetic methods. In J. F. Bussiere, J. P. Monchalin, C. O. Ruud and R. E. Green, Jr., (eds.), *Nondestructive Characterization of Materials II,* New York: Plenum, 1987, pp. 211–225.
5. K. Tiitto, Use of Barkhausen effect in testing for residual stresses and defects. In W. B. Young (ed.), *Residual Stress in Design, Process, and Materials Selection,* Metals Park OH: ASM Int'l 1987, pp. 27–36.
6. D. C. Jiles, Review of magnetic methods for nondestructive evaluation, *NDT International,* **21**: 311–319, 1988.
7. R. E. Beissner, Magnetic field testing. In S. R. Lampman and T. B. Zorc (eds.), *Metals Handbook,* Vol. 17, Metals Park, OH: ASM Int'l, 1989, pp. 129–135.
8. W. L. Rollwitz, Magaborption NDE. In S. R. Lampman and T. B. Zorc (eds.), *Metals Handbook,* Vol. 17, Metals Park, OH: ASM Int'l 1989, pp. 144–158.
9. H. Kwun and G. L. Burkhardt, Electromagnetic techniques for residual stress measurements. In S. R. Lampman and T. B. Zorc (eds.), *Metals Handbook,* Vol. 17, Metals Park, OH: ASM Int'l, 1989, pp. 159–163.
10. D. C. Jiles, Review of magnetic methods of nondestructive evaluation (Part 2), *NDT International,* **23**: 83–92, 1990.
11. J. Lamontanara et al., Monitoring fatigue damage in industrial steel by Barkhausen noise, *Nondestr. Test. Eval.,* **8–9**: 603–614, 1992.
12. D. J. Buttle and T. M. Hutchings, Residual stress measurement at NNDTC, *Brit. J. NDT (now Insight)* **34**: 175–182, 1992.
13. M. K. Devine, The magnetic detection of material properties, *J. Metals,* 24–30, Oct. 1992.
14. H. Kwun, Application of magnetically induced velocity changes of ultrasonic waves for NDE of material properties, *Nondestr. Test. Eval.,* **10**: 127–136, 1992.
15. C. B. Scruby et al., Development of non-invasive methods for measurement of stress in welded steel structures, *Eur. J. NDT,* **3** (2): 46–54, 1993.
16. R. A. Langman and P. J. Mutton, Estimation of residual stresses in railway wheels by means of stress-induced magnetic anisotropy, *NDT&E International,* **26**: 195–205, 1993.
17. M. J. Sablik, Hysteresis modeling of the effects of stress on magnetic properties and its application to Barkhausen NDE. In *Current Topics in Magnetics Research,* Vol. 1, Trivandrum, India: Research Trends, 1994, pp. 45–57.
18. M. J. Sablik, Modeling the effects of biaxial stress on magnetic properties of steels with application to biaxial stress NDE, *Nondestr. Test. Eval.,* **12**: 87–102, 1995.
19. M. J. Sablik and D. C. Jiles, Magnetic measurement of creep damage: modeling and experiment. In M. Prager and R. E. Tilley (eds.), *Nondestructive Evaluation of Utilities and Pipelines,* Vol. 2947, SPIE Proc., Bellingham, WA: SPIE, 1996, pp. 166–176.
20. J. A. Alcoz, S. Nair, and M. J. Sablik, Electromagnetic methods for stress measurement, *Nondestructive Testing Handbook,* Vol. 9, R. K. Stanley and P. O. Moore (eds.), Columbus, OH: ANST, 1996, pp. 421–430.
21. C. E. Betz, *Principles of Magnetic Particle Testing,* Chicago: Magnaflux Corp., 1967.
22. P. A. Tipler, *Physics,* New York: Worth Publishers, 1976, p. 858.
23. Y. F. Cheu, Automatic crack detection with computer vision and pattern recognition of magnetic particle indicators, *Mater. Eval.,* **42**: 1506–1511, 1984.
24. F. Forster, Developments in magnetography of tubes and tube welds, *Nondestructive Testing,* **8**: 304–308, 1975.
25. C. H. Hastings, A new type of flaw detector, *ASTM Proc.,* **47**: 651–664, 1947.
26. K. F. Bainton, Characterizing defects by determining leakage fields, *NDT International,* **10**: 253–257, 1977.

27. R. E. Beissner, G. A. Matzkanin, and C. M. Teller, NDE application of magnetic leakage field methods. *SwRI Report NTIAC-80-1,* NTIAC, Southwest Research Institute, San Antonio, TX, 1980.

28. M. J. Sablik and R. E. Beissner, Theory of magnetic leakage fields from prolate and oblate spheroidal inclusions, *J. Appl. Phys.,* **53**: 8437–8450, 1982.

29. T. A. Bubenik et al., Magnetic flux leakage (MFL) technology for natural gas pipeline inspection, *Gas Research Institute Report 91-0367,* GRI, Chicago, IL, 1992.

30. P. A. Khalileev and P. A. Grigorev, Methods of testing the condition of underground pipes in main pipelines, *Sov. J. NDT,* **10**: 438–459, 1974.

31. N. N. Zatsepin and V. E. Shcherbinin, Calculation of the magnetic field of surface defects, I. Field topography of defect models, *Sov. J. NDT,* **2**: 385–393, 1966.

32. V. E. Shcherbinin and N. N. Zatsepin, Calculation of the magnetic field of surface defects, II. Experimental verification of the principal theoretical relationships, *Sov. J. NDT,* **2**: 394–399, 1966.

33. C. Edwards and S. B. Palmer, The magnetic field of surface breaking cracks, *J. Phys. D,* **19**: 657–673, 1986.

34. J. H. Hwang and W. Lord, Finite element modeling of magnetic field-defect interactions, *J. Test. Eval.,* **3**:21–25, 1975.

35. W. Lord et al., Residual and active leakage fields around defects in ferromagnetic materials, *Mater. Eval.,* **36**: 47–54, July 1978.

36. D. L. Atherton and W. Czura, Finite element calculations on the effect of permeability variation on magnetic flux leakage signals, *NDT Int.,* **20**: 239–241, 1987.

37. D. L. Atherton, Finite element calculations and computer measurements of magnetic flux leakage patterns for pits, *Brit. J. NDT,* **30**: 159–162, 1988.

38. B. Brudar, Magnetic leakage fields calculated by the method of finite differences, *NDT Int.,* **18**: 353–357, 1985.

39. G. Dobmann, Magnetic leakage flux techniques in NDT: a state of the art survey of the capabilities for defect detection and sizing. In W. Lord (ed.), *Electromagnetic Methods of NDT,* New York: Gordon and Breach, 1985, pp. 71–95.

40. P. Holler and G. Dobmann, Physical analysis methods of magnetic flux leakage. In R. S. Sharpe (ed.), *Res. Techniques NDT,* Vol. IV, New York: Academic Press, 1980, pp. 39–69.

41. C. N. Owston, The magnetic flux leakage technique of nondestructive testing, *Brit. J. NDT,* **16**: 162–168, 1974.

42. F. Forster, New findings in the fields of nondestructive magnetic field leakage inspection, *NDT Int.,* **19**: 3–14, 1986.

43. R. E. Beissner et al., Analysis of mechanical damage detection in gas pipeline inspection, *Proc. Conf. Prop. Applic. Magnetic Materials,* Illinois Institute of Technology, Chicago, IL, May 1996.

44. T. W. Krause et al., Variation of the stress dependent magnetic flux leakage signal with defection depth and flux density, *N.D.T.&E. Int.,* **29**: 79–86, 1996.

45. T. W. Krause et al., Effect of stress concentration on magnetic flux leakage signals from blind hole defects in stressed pipeline steel, *Res. Nondestr. Eval.,* **8**: 83–100, 1996.

46. R. E. Beissner et al., Detection and analysis of electric current perturbation caused by defects. In G. Birnbaum and G. Free (eds.), *Eddy Current Characterization of Materials and Structures,* ASTM ATP 722, Philadelphia: ASTM, 1981, pp. 428–446.

47. R. E. Beissner, M. J. Sablik, and C. M. Teller, Electric current perturbation calculations for half-penny cracks. In D. O. Thompson and D. E. Chimenti (eds.), *Rev. Progr. In Quant. NDE,* Vol. 2B, New York: Plenum, 1983, pp. 1237–1254.

48. J. A. Birdwell, F. N. Kusenberger, and J. R. Barton, Development of magnetic perturbation inspection system (A02G5005-1) for CH-46 rotor blades, *P.A. No. CA375118,* Technical Summary Report for Vertol Division, The Boeing Company, 1968.

49. J. R. Barton, J. Lankford, and P. L. Hampton, Advanced nondestructive testing methods for bearing inspection, *SAE Trans.,* **81**: 681–696, 1972.

50. H. Kwun and C. M. Teller, Nondestructive evaluation of pipes and tubes using magnetostrictive sensors, U.S. Patent No. 5,581,037, December 1996.

51. H. Kwun, J. J. Hanley, and C. M. Teller, Performance of a noncontact magnetostrictive AE sensor on steel rod, *J. Acoust. Emission,* **11**: 27–31, 1993.

52. H. Kwun and A. E. Holt, Feasibility of underlagging corrosion detection in steel pipe using the magnetostrictive sensor technique, *NDT&E Int.,* **28**: 211–214, 1995.

53. H. Kwun and J. J. Hanley, Long-range, volumetric inspection of tubing using the magnetostrictive sensor technique, *Proc. 4th EPRI Balance-of-Plant Heat Exchanger NDE Symposium,* Jackson Hole, Wyoming, 1996.

54. H. Kwun and C. M. Teller, Detection of fractured wires in steel cables using magnetostrictive sensors, *Mater. Eval.,* **52**: 503–507, 1994.

55. K. A. Bartels, H. Kwun, and J. J. Hanley, Magnetostrictive sensors for the characterization of corrosion in rebars and prestressing strands. In *Nondestructive Evaluation of Bridges and Highways,* SPIE Conf. Proc. 2946, SPIE, Bellingham, WA, 1996, pp. 40–50.

56. H. Kwun, Back in style: magnetostrictive sensor, *Technology Today,* Southwest Research Institute, San Antonio, TX, Mar. 1995, pp. 2–7.

57. V. G. Kuleev, P. S. Kononov, and I. A. Telegina, Electromagnetoacoustic excitation of elastic longitudinal cylindrical waves in ferromagnetic bars, *Sov. J. NDT,* **19**: 690–698, 1983.

58. V. D. Boltachev et al., Electromagnetic-acoustic excitation in ferromagnetic pipes with a circular cross-section, *Sov. J. NDT,* **25**: 434–439, 1989.

59. M. J. Sablik and S. W. Rubin, Modeling magnetostrictive generation of elastic waves in steel pipes. I. Theory, *Int. J. Appl. Electromagnetics and Mechanics,* submitted 1998.

60. H. Kwun and K. A. Bartels, Experimental observation of elastic waves dispersion in bounded solids of various configurations. *J. Acoust. Soc. Am.,* **99**: 962–968, 1996.

61. M. J. Sablik, Y. Lu, and G. L. Burkhardt, Modeling magnetostrictive generation of elastic waves in steel pipes. II. Comparison to experiment, *Int. J. Appl. Electromagn. Mech.* submitted 1998.

62. M. J. Sablik and R. A. Langman, Approach to the anhysteretic surface, *J. Appl. Phys.,* **79**: 6134–6136, 1996.

63. S. Chikazumi and S. H. Charap, *Physics of Magnetism,* Malabar, FL: R. E. Krieger Publ. Co., 1984, pp. 19–24.

64. M. N. Mikheev, Magnetic structure analysis, *Sov. J. NDT,* **19**: 1–7, 1983.

65. M. N. Mikheev et al., Interrelation of the magnetic and mechanical properties with the structural state of hardened and tempered products, *Sov. J. NDT,* **18**: 725–732, 1983.

66. H. Kwun and G. L. Burkhardt, Effects of grain size, hardness and stress on the magnetic hysteresis loops of ferromagnetic steels. *J. Appl. Phys.,* **61**: 1576–1579, 1987.

67. R. Ranjan, D. C. Jiles, and P. K. Rastogi, Magnetoacoustic emission, magnetization and Barkhausen effect in decarburized steel, *IEEE Trans. Magn.,* **22**: 511–513, 1986.

68. R. Ranjan, D. C. Jiles, and P. K. Rastogi, Magnetic properties of decarburized steels: an investigation of the effects of grain

size and carbon content, *IEEE Trans. Magn.,* **23**: 1869–1876, 1987.

69. Z. J. Chen et al., Assessment of creep damage of ferromagnetic material using magnetic inspection, *IEEE Trans. Magn.,* **30**: 4596–4598, 1994.
70. D. C. Jiles and D. L. Atherton, Theory of ferromagnetic hysteresis. *J. Magn. Magn. Mater.,* **6**: 48–61, 1986.
71. M. J. Sablik et al., Finite element simulation of magnetic detection of creep damage at seam welds, *IEEE Trans. Magn.,* **32**: 4290–4292, 1996.
72. Z. J. Chen, D. C. Jiles, and J. Kameda, Estimate of fatigue exposure from magnetic coercivity, *J. Appl. Phys.,* **75**: 6975–6977, 1994.
73. Z. Gao et al., Variation of coercivity of ferromagnetic material during cyclic stressing, *IEEE Trans. Magn.,* **30**: 4593–4595, 1994.
74. L. J. Swartzendruber et al., Effect of plastic strain on magnetic and mechanical properties of ultraslow carbon sheet steel, *J. Appl. Phys.,* **81**: 4263–4265, 1997.
75. H. Barkhausen, Two phenomena revealed with help of new amplifiers. *Pzysikalischte Zeitschrift,* **20**: 401–403, 1919.
76. K. Stierstadt, The magnetic Barkhausen effect. In *Springer Tracts in Modern Physics,* **40**: 2–106, 1966 (in German).
77. J. C. McClure and K. Schröder, The magnetic Barkhausen effect, *CRC Critical Reviews in Solid State Sciences,* **6**: 45–83, 1976.
78. G. A. Matzkanin, R. E. Beissner, and C. M. Teller, The Barkhausen effect and its applications to nondestructive evaluation, *SWRI Report No NTIAC-79-2,* 1979.
79. S. Segalini, M. Mayos, and M. Putignani, Application of electromagnetic methods to steel microstructure control. *Memoires et Etudes Scientifique, Revue de Metallurgie,* October 1985, pp. 569–575 (in French).
80. W. L. Vengrinovich, Magnetic noise spectroscopy, In *Minsk-Science,* Minsk, 1991, 284 pp (in Russian).
81. T. Piech, Technical application of Barkhausen effect, *PNPS 475,* ISSN 0208-7979, Technical University of Szczecin, Szczecin, 1992, 160 pp (in German).
82. A. Zentkova and M. Datko, Propagation of the electrodynamic disturbance following a Barkhausen jump in metallic ferromagnetic samples. I Infinite medium, *Czech, J. Phys.,* **B24**: 310–321, 1974.
83. V. M. Vasiliev et al., Some computation and design problems of induction transducers for the detection of Barkhausen jumps, *Defektscopiya,* **2**: 73–83, 1986.
84. B. Augustyniak, Magnetomechanical effects, *Rapport TEMPRA,* GEMPPM, INSA de Lyon, 1995, 90 pp (in French).
85. J. Mackersie, R. Hill, and A. Cowking, Models for acoustic and electromagnetic Barkhausen emission. In J. Boogaard and G. M. van Dijk (eds), *Non-Destr. Test. Proc. 12th World Conf.,* Amsterdam: Elsevier Science Publ., 1989, pp. 1515–1518.
86. M. M. Kwan, K. Ono, and M. Shibata, Magnetomechanical acoustic emission of ferromagnetic materials at low magnetization levels (type I behavior), *J. Acoustic Emission,* **3**: 144–156, 1984.
87. M. M. Kwan, K. Ono, and M. Tibet, Magnetomechanical acoustic emission of ferromagnetic materials at low magnetization levels (type II behavior), *J. Acoustic Emission,* **3**: 199–210, 1984.
88. M. Guyot, T. Merceron, and C. Cagan, Acoustic emission along the hysteresis loops of various ferro- and ferrimagnets, *J. Appl. Phys.,* **63**: 3955–3957, 1988.
89. B. Augustyniak, Magnetomechanical emission. *Acoustic Emission,* J. Malecki, J. Ranachowski (eds.), IPPT-PAN Warsaw, 1994, pp. 417–445 (in Polish).
90. A. D. Beale et al., Micromagnetic processes in steels, *Mat. Res. Soc. Symp. Proc.,* Materials Research Society, 1991, pp 313–318.
91. D. G. Hwang and H. C. Kim, The influence of plastic deformation on Barkhausen effects and magnetic properties in mild steel, *J. Phys. D.,* **21**: 1807–1813, 1988.
92. B. Alessandro et al., Domain-wall dynamics and Barkhausen effect in metallic ferromagnetic materials, I. Theory, *J. Appl. Phys.,* **68**: 2901–2907, 1990.
93. B. Alessandro et al., Domain-wall dynamics and Barkhausen effect in metallic ferromagnetic materials. II. Experiments, *J. Appl. Phys.,* **68**: 2908–2915, 1990.
94. H. C. Kim, D. G. Hwang, and B. K. Choi, Barkhausen noise in 5% Mo-75.5% Ni permalloy with rolling texture, *J. Phys. D.,* **21**: 168–174, 1988.
95. B. Augustyniak, Magnetomechanical effects research for their application in nondestructive evaluation of ferromagetic materials, *Rapport ATP de France,* Nr 717, Technical University of Gdansk, 1996 (in French).
96. L. Basano and P. Ottonello, Use of time-day correlators and wave-shaping techniques in the statistical analysis of Barkhausen pulses, *J. Magn. Magn. Mater.,* **43**: 274–282, 1994.
97. C. Gatelier-Rothea et al., Role of microstructural states on the level of Barkhausen noise inpure iron and low carbon iron binary alloys: *Nondestructive Test. Eval.,* **8–9**: 591–602, 1992.
98. D. J. Buttle et al., Magnetoacoustic and Barkhausen emission in ferromagnetic materials, *Philos. Trans. R. Soc. London,* **A320**: 363–378, 1986.
99. B. Augustyniak and J. Degauque, New approach to hysteresis process investigation using mechanical and magnetic Barkhausen effects, *J. Magn. Magn. Mater.,* **140–144**: 1837–1838, 1995.
100. American Stress Technologies, Inc. Stresscan 500 C operating instructions, Pittsburgh Pennsylvania, 1988.
101. B. Augustyniak, M. Chmielewski, and W. Kielczynski, New method of residual stress evaluation in weld seams by means of Barkhausen effect, *Proc. XXIV National Conf. NDE,* PTBN i DT, Poznan-Kiekrz, 1995, pp. 9–17 (in Polish).
102. D. C. Jiles, Integrated on-line instrumentation for simultaneous automated measurements of magnetic field, induction, Barkhausen effect, magnetoacoustic emission, and magnetostriction, *J. Appl. Phys.,* **63**: 3946–3949, 1988.
103. A. Parakka and D. C. Jiles, Magnetoprobe: a portable system for non-destructive testing of ferromagnetic materials, *J. Magn. Magn. Mater,* **140–144**: 1841–1842, 1995.
104. H. Sakamoto, M. Okada, and M. Homma, Theoretical analysis of Barkhausen noise in carbon steels, *IEEE Trans. Magn.,* **23**: 2236–2238, 1987.
105. D. J. Buttle et al., Magneto-acoustic and Barkhausen emission from domain-wall interaction with precipitates in incolay 904, *Philos. Mag. A,* **55**: 735–756, 1987.
106. R. Rautioaho, P. Karjalainen, and M. Moilanen, Coercivity and power spectrum of Barkhausen noise in structural steels, *J. Magn. Magn. Mater.,* **61**: 183–192, 1986.
107. R. Ranjan et al., Grain size measurement using magnetic and acoustic Barkhausen noise, *J. Appl. Phys.,* **61**: 3199–3201, 1987.
108. S. Tiitto, Magnetoelastic Barkhausen noise method for testing of residual stresses. American Stress Technologies, Inc., Pittsburgh, PA, 1989.
109. G. Bertotti, F. Fiorillo, and A. Montorsi, The role of grain size in the magnetization process of soft magnetic materials, *J. Appl. Phys.,* **67**: 5574–5576, 1990.
110. M. Komatsubara and J. L. Porteseil, Barkhausen noise behavior in grain oriented 3% SiFe and the effect of local strain, *IEEE Trans. Magn.,* **MAG-22**: 496–498, 1986.

111. T. W. Krause et al., Correlation of magnetic Barkhausen noise with core loss in oriented 3% Si-Fe steel laminates, *J. Appl. Phys.,* **79**: 3156–3167, 1996.
112. D. J. Buttle et al., Magneto-acoustic and Barkhausen emission: their dependence on dislocations in iron, *Philos. Mag. A,* **55**: 717–734, 1987.
113. A. J. Birkett et al., Influence of plastic deformation on Barkhausen power spectra in steels, *J. Phys. D,* **22**: 1240–1242, 1989.
114. C. Bach, K. Goebbels, and W. Theiner, Characterization of hardening depth by Barkhausen noise measurements, *Mater. Eval.,* **46**: 1576–1580, 1988.
115. L. Malkinski, Z. Kaczkowski, and B. Augustyniak, Application of Barkhausen effect measurements in piezomagnetic study of metallic glasses, *J. Magn. Magn. Mater.,* **112**: 323–324, 1992.
116. B. Augustyniak and J. Degauque, Microstructure inspection by means of mechanical Barkhausen effect analysis, *J. de Physique,* IV, **C8**: 527–530, 1996.
117. P. Deimel et al., Bloch wall arrangement and Barkhausen noise in steels 22 NiMoCr 3 7 and 15 MnMoNiV 5 3, *J. Magn. Mater.,* **36**: 277–289, 1983.
118. B. Augustyniak, Results of recent progress in new NDT methods of ferromagnetic materials, *IFTR Reports IPPT PAN Warsaw 1996,* 1/1996 (in Polish).
119. Z. J. Chen, A. Strom, and D. C. Jiles, Micromagnetic surface measurements for evaluation of surface modifications due to cyclic stress, *IEEE Trans. Magn.,* **29**: 3031–3033, 1993.
120. P. Gondi et al., Structural characteristics at surface and Barkhausen noise in AISI 4340 steel after grinding, *Nondestr. Test. Eval.,* **10**: 255–267, 1993.
121. W. A. Theiner and V. Hauk, Nondestructive characterization of shot peened surface states by the magnetic Barkhausen noise method. In J. Boogaard and G. M. van Dijk (eds.), *Non-Destr. Test., Proc. 12th World Conf.,* Amsterdam: Elsevier, 1989, pp. 583–587.
122. J. C. McClure Jr., S. Bhattacharya, and K. Schröder, Correlation of Barkhausen effect type measurements with acoustic emission in fatigue crack growth studies, *IEEE Trans. Magn.,* **MAG-10**: 913–915, 1974.
123. S. Battacharya and K. Schröder, A new method of detecting fatigue crack propagation in ferromagnetic specimens, *J. Test. Eval.,* **3**: 289–291, 1975.
124. S. Nishimura and K. Tokimasa, Study on the residual stresses in railroad solid wheels and their effect on wheel fracture, *Bull. JSME,* **19**: 459–468, 1976.
125. J. F. Shackelford and B. D. Brown, A critical review of residual stress technology, *Intl. Adv. NDT,* **15**: 195–215, 1990.
126. R. M. Bozorth, *Ferromagnetism,* Chap. 13, NJ: AT&T, 1978 (reprinted from 1951), pp. 595–712.
127. R. M. Bozorth and H. J. Williams, Effect of small stresses on magnetic properties, *Rev. Mod. Phys.,* **17**: 72–80, 1945.
128. D. J. Craik and M. J. Wood, Magnetization changes induced by stress in a constant applied field, *J. Phys. D,* **3**: 1009–1016, 1970.
129. A. J. Moses, Effect of stress on d.c. magnetization properties of permendur, *Proc. IEE,* **122**: 761–762, 1975.
130. R. Langman, Measurement of the mechanical stress in mild steel by means of rotation of magnetic field strength, *NDT Int.,* **14**: 255–262, 1981.
131. R. Langman, The effect of stress on the magnetization of mild steel at moderate field strengths, *IEEE Trans. Magn.,* **21**: 1314–1320, 1985.
132. M. J. Sablik et al., Model for the effect of tensile and compressive stress on ferromagnetic hysteresis, *J. Appl. Phys.,* **61**: 3799–3801, 1987.
133. I. J. Garshelis, Magnetic and magnetoelastic properties of nickel maraging steels, *IEEE Trans. Magn.,* **26**: 1981–1983, 1990.
134. H. Hauser and P. Fulmek, The effect of mechanical stress on the magnetization curves of Ni and FeSi single crystals at strong fields, *IEEE Trans. Magn.,* **28**: 1815–1825, 1992.
135. C. S. Schneider, P. Y. Cannell, and K. T. Watts, Magnetoelasticity for large stresses, *IEEE Trans. Magn.,* **28**: 2626–2631, 1992.
136. M. J. Sablik and D. C. Jiles, Coupled magnetoelastic theory of magnetic and magnetostrictive hysteresis, *IEEE Trans. Magn.,* **29**: 2113–2123, 1993.
137. M. J. Sablik et al., A model for hysteretic magnetic properties under the application of noncoaxial stress and field, *J. Appl. Phys.,* **74**: 480–488, 1993.
138. H. Kwun, Investigation of the dependence of Barkhausen noise on stress and the angle between the stress and magnetization direction, *J. Magn. Magn. Mater.,* **49**: 235–240, 1985.
139. R. Langman, Measurement of the mechanical stress in mild steel by means of rotation of magnetic field strength—Part 2: Biaxial stress, *NDT Int.,* **15**: 91–97, Apr. 1982.
140. C. S. Schneider and J. M. Richardson, Biaxial magnetoelasticity in steels, *J. Appl. Phys.,* **53**: 8136–8138, 1982.
141. D. J. Buttle et al., Comparison of three magnetic techniques for biaxial stress measurement. In D. O. Thompson and D. E. Chimenti (eds.), *Rev. Progr. In Quant. NDE,* Vol. 9, New York: Plenum, 1990, pp. 1879–1885.
142. R. Langman, Magnetic properties of mild steel under conditions of biaxial stress, *IEEE Trans. Magn.,* **26**: 1246–1251, 1990.
143. K. Kashiwaya, Fundamentals of nondestructive measurement of biaxial stress in steel utilizing magnetoelastic effect under low magnetic field, *Jap. J. Appl. Phys.,* **30** (11A): 2932–2942, 1991.
144. M. J. Sablik et al., Micromagnetic model for biaxial stress effects on magnetic properties, *J. Magn. Magn. Mater.,* **132**: 131–148, 1994.
145. M. J. Sablik, H. Kwun, and G. L. Burkhardt, Biaxial stress effects on hysteresis and MIVC, *J. Magn. Magn. Mater.,* **140–144**: 1871–1872, 1995.
146. M. J. Sablik, R. A. Langman, and A. Belle, Nondestructive magnetic measurement of biaxial stress using magnetic fields parallel and perpendicular to the stress plane. In D. O. Thompson and D. E. Chimenti (eds.), *Rev. Progr. In Quant. NDE,* Vol. 16B, New York: Plenum, 1997, pp. 1655–1662.
147. M. J. Sablik, A model for asymmetry in magnetic property behavior under tensile and compressive stress in steel, *IEEE Trans. Magn.* **33**: 3958–3960, 1997.
148. C. S. Schneider and M. Charlesworth, Magnetoelastic processes in steel, *J. Appl. Phys.,* **57**: 4196–4198, 1985.
149. H. Hauser, Energetic model of ferromagnetic hysteresis, *J. Appl. Phys.,* **75**: 2584–2597, 1994.
150. H, Hauser, Energetic model of ferromagnetic hysteresis. 2. Magnetization calculations of (110)[001] FeSi sheets by statistic domain behavior, *J. Appl. Phys.,* **77**: 2625–2633, 1995.
151. I. J. Garshelis and W. S. Fiegel, Recovery of magnetostriction values from the stress dependence of Young's modulus, *IEEE Trans. Magn.,* **22**: 436–438, 1986.
152. W. F. Brown, Jr., Domain theory of ferromagnetics under stress, part I, *Phys. Rev.,* **52**: 325–334, 1937.
153. W. F. Brown, Jr., Domain theory of ferromagnetics under stress, part II, *Phys. Rev.,* **53**: 482–489, 1938.
154. G. W. Smith and J. R. Birchak, Internal stress distribution theory of magnetomechanical hysteresis—an extension to include effects of magnetic field and applied stress, *J. Appl. Phys.,* **40**: 5174–5178, 1969.

155. L. Callegaro and E. Puppin, Rotational hysteresis model for stressed ferromagnetic films, *IEEE Trans. Magn.,* **33**: 1007–1011, 1997.

156. A. Bienkowski and J. Kulikowski, The dependence of the Villari effect in ferrites on their magnetocrystalline properties and magnetostriction, *J. Magn. Magn. Mater.,* **26**: 292–294, 1982.

157. E. Villari, Change of magnetization by tension and by electric current, *Ann. Phys. Chem.,* **126**: 87–122, 1865.

158. M. J. Sablik et al., A model for the effect of stress on the low frequency harmonic content of the magnetic induction in ferromagnetic materials, *J. Appl. Phys.,* **63**: 3930–3932, 1988.

159. Z. J. Chen et al., Improvement of magnetic interface coupling through a magnetic coupling gel, *IEEE Trans. Magn.,* **31**: 4029–4031, 1995.

160. R. E. Ershov and M. M. Shel, On stress measurement by means of the magnetoelastic method, *Industrial Laboratory,* **31**: 1008–1011, 1965.

161. S. Abiku and B. D. Cullity, A magnetic method for the determination of residual stress, *Experimental Mech.,* **11**: 217–223, 1971.

162. S. Abiku, Magnetic studies of residual stress in iron and steel induced by uniaxial deformation, *Jap. J. Appl. Phys.,* **16**: 1161–1170, 1977.

163. S. A. Musikhin, V. F. Novikov, and V. N. Borsenko, Use of coercive force as an indicator parameter in nondestructive measurement of mechanical stresses, *Sov. J. NDT,* **23**: 633–635, 1988.

164. M. K. Devine, Detection of stress in railroad steels via magnetic property measurements, *Nondestr. Test. Eval.,* **11**: 215–234, 1994.

165. H. Kwun and G. L. Burkhardt, Effects of stress on the harmonic content of magnetic induction in ferromagnetic material, *Proc. 2nd Nat'l Seminar NDE Ferromagnetic Materials,* Dresser-Atlas, Houston, TX, 1986.

166. H. Kwun and G. L. Burkhardt, Nondestructive measurement of stress in ferromagnetic steels using harmonic analysis of induced voltage, *NDT Int.,* **20**: 167–171, 1987.

167. G. L. Burkhardt and H. Kwun, Application of the nonlinear harmonics method to continuous measurement of stress in railroad rail. In D. O. Thompson and D. E. Chimenti (eds.), *Rev. Progr. Quant. NDE,* Vol. 7B, New York: Plenum, 1988, pp. 1413–1420.

168. H. Kwun, G. L. Burkhardt, and M. E. Smith, Measurement of the longitudinal stress in railroad rail under field conditions using nonlinear harmonics. In D. O. Thompson and D. E. Chimenti, (eds.), *Rev. Progr. Quant. NDE,* Vol. 9, New York: Plenum, 1990, pp. 1895–1903.

169. R. Langman, Measurements of the mechanical stress in mild steel by means of rotation of magnetic field strength—part 3. Practical applications, *NDT Int.,* **16**: 59–65, 1983.

170. R. Langman, Some comparisons between the measurement of stress in mild steel by means of Barkhausen noise and by rotation of magnetization, *NDT Int.,* **20**: 93–99, 1987.

171. K. Kashiwaya, H. Sakamoto, and Y. Inoue, Nondestructive measurement of residual stress using magnetic sensors, *Proc. VI Intl. Congress Experimental Mech.,* Society for Experimental Mechanics, Bethel, CT, 1977, Vol. I, pp. 30–35.

172. H. Wakiwaka, M. Kobayashi, and H. Yamada, Stress measurement using a magnetic anisotropy sensor utilizing ac magnetization, *IEEE Transl. J. Magn. in Japan,* **6**: 396–401, 1991.

173. S. Kishimoto et al., Conversion theory of magnetic anisotropy sensor, *IEEE Trans. J. Magn. in Japan,* **7**: 269–273, 1992.

174. K. Kashiwaya, Y. Inoue, and H. Sakamoto, Development of magnetic anisotropy sensor for stress measurement of curved surface. In J. Boogaard and G. M. Van Dijk (eds.), *Proc. 12th World Conf. On Non-Destructive Testing,* Amsterdam: Elsevier, 1989, pp. 601–606.

175. H. Kwun and C. M. Teller, Stress dependence of magnetically induced ultrasonic shear wave velocity change in polycrystalline A-36 steel, *J. Appl. Phys.,* **54**: 4856–4863, 1983.

176. H. Kwun, Effects of stress on magnetically induced velocity changes for ultrasonic longitudinal waves in steel, *J. Appl. Phys.,* **57**: 1555–1561, 1985.

177. H. Kwun, A nondestructive measurement of residual bulk stresses in welded steel specimens by use of magnetically induced velocity changes for ultrasonic waves, *Mater. Eval.,* **44**: 1560–1566, 1986.

178. M. Namkung and D. Utrata, Nondestructive residual stress measurements in railroad wheels using the low-field magnetoacoustic test method. In D. O. Thompson and D. E. Chimenti (eds.), *Rev. Progr. Quant. NDE,* Vol. 7B, New York: Plenum, 1988, pp. 1429–1438.

179. M. Shibata and K. Ono, Magnetomechanical acoustic emission—a new method for non-destructive stress measurements, *NDT Int.,* **14**: 227–234, 1981.

180. G. L. Burkhardt et al., Acoustic methods for obtaining Barkhausen noise stress measurements, *Mater. Eval.,* **40**: 669–675, 1982.

181. R. Rautioaho, P. Karjalajnen, and M. Moilajnen, The statistical contribution of magnetic parameters to stress measurements by Barkhausen noise. In H. Fujiwara, T. Abe, and K. Tanaka (eds.), *Residual Stresses-III, Science and Technology,* Vol. 2, London: Elsevier, 1989, pp. 1087–1092.

182. D. J. Buttle et al., The measurement of stress in steels of varying microstructure by magnetoacoustic and Barkhausen emission, *Proc. R. Soc. London,* Ser. A, **414**: 469–496, 1987.

183. M. Nankung et al., Uniaxial stress effects on magnetoacoustic emission. In B. R. McAvoy (ed.), *Proc. IEEE 1989 Ultrasonics Symposium,* Montreal 1989, Vol. 2, [IEEE 1089], pp. 1167–1170

184. C. Jagadish, L. Clapham, and D. L. Atherton, Influence of uniaxial elastic stress on power spectrum and pulse height distribution of surface Barkhausen noise in pipeline steel, *IEEE Trans. Magn.,* **26**: 1160–1163, 1990.

185. M. G. Maylin and P. T. Squire, The effects of stress on induction, differential permeability and Barkhausen count in a ferromagnet, *IEEE Trans. Magn.,* **26**: 3499–3501, 1993.

186. M. J. Sablik, A model for the Barkhausen noise power as a function of applied magnetic field and stress, *J. Appl. Phys.,* **74**: 5898–5900, 1993.

187. M. J. Sablik and B. Augustyniak, The effect of mechanical stress on a Barkhausen noise signal integrated across a cycle of ramped magnetic field, *J. Appl. Phys.,* **79**: 963–972, 1996.

188. T. Piech, Application of the Barkhausen effect to mechanical stress measurements in ferromagnetics. In E. Czoboly (ed.), *Proc. 9th Congress of Materials Testing,* Budapest 1986, Vol. 2, 1986, pp. 495–496.

189. S. Tiitto, Magnetoelastic testing of biaxial stresses, *Experimental Techniques,* pp. 17–22, July/August 1991.

190. W. A. Theiner and P. Deimel, Non-destructive testing of welds with the 3MA-analyzer, *Nucl. Eng. Design,* **102**: 257–264, 1987.

191. K. Tiitto et al., Evaluation of the stress distribution in welded steel by measurement on the Barkhausen noise level, *Proc. Conf. Practical Applic. Residual Stress Technology,* Indianapolis 1991, pp. 55–59.

192. B. Augustyniak, New approach in Barkhausen effect application to residual stress evaluation, *Nondestr. Testing,* Polish Society for NDT, **5**: 17, 1996 (in Polish).

193. B. Augustyniak and W. Kielczynski, Comparison of non-destructive methods of residual stress evaluation in weld seams, *Proc.*

25th Nat'l Conf. on NDT, Szczyrk 1996, PTBN&DT SIMP, Warsaw 1996, Zeszyty Problemowe, 1, 235, 1996 (in Polish).

194. C. Jagadish, L. Clapham, and D. L. Atherton, Effect of bias field and stress on Barkhausen noise in pipeline steels, *NDT Int.,* **22**: 297–301, 1989.
195. R. L. Pasley, Barkhausen effect—an indication of stress, *Mater. Eval.,* **28**: 157–161, 1970.
196. W. A. Theiner and H. H. Willems, Determination of microstructural parameters by magnetic and ultrasonic quantitative NDE. In C. O. Ruud and R. E. Green, Jr., (eds.), *Nondestr. Methods for Mater. Property Determination,* New York: Plenum, 1984, pp. 249–258.
197. M. J. Sablik, W. L. Rollwitz, and D. C. Jiles, A model for magabsorption as an NDE tool for stress measurement, *Proc. 17th Symp. on NDE,* San Antonio, TX, NTIAC, Southwest Research Institute, San Antonio, TX, 1989, pp. 212–223.
198. K. Babcock et al., Magnetic force microscopy: recent advances and applications. In D. G. Demczyk, E. Garfunkel, B. M. Clemens, E. D. Williams, and J. J. Cuomo (eds.), *Evol. of Thin Film and Surf. Struct. and Morphology,* MRS Proceedings, Vol. 335, Pittsburgh: Materials Research Society, 1995, pp. 311–321.
199. A. C. Bruno, C. H. Barbarosa, and L. F. Scavarda, Electric current injection NDE using a SQUID magnetometer, *Res. Nondestr. Eval.,* **8**: 165–175, 1996.
200. M. Lang et al., Characterization of the fatigue behavior of austenitic steel using HTSC-SQUID, *QNDE Conference,* Univ. San Diego, San Diego, CA, July 1997.

M. J. SABLIK
Southwest Research Institute

B. AUGUSTYNIAK
Technical University of Gdansk